A High-Resolution Aerial Survey and Radar Analysis of Quasi-Linear Convective System Surface Vortex Damage Paths from 31 August 2014

KEVIN D. SKOW AND CRAIG COGIL

NOAA/NWS/Des Moines Weather Forecast Office, Johnston, Iowa

ABSTRACT

On the evening of 31 August 2014, a powerful quasi-linear convective system (QLCS) impacted much of Iowa. In the weeks following the event, the entire path of the QLCS was imaged at ~1-m resolution using aerial photography through the National Agriculture Imagery Program. The predominantly flat, mature agricultural land cover of central Iowa provided an excellent medium on which to document wind phenomena of varying scales. The high-resolution aerial data, in combination with recent spatial, temporal, and polarimetric upgrades to the Weather Surveillance Radar-1988 Doppler (WSR-88D) network, offer an extraordinary glimpse into the quantity, evolution, and scale of surface vortices generated throughout the entire lifespan of this QLCS. One hundred eleven damage tracks associated with these vortices were cataloged along the storm's 350-km path, ranging in length from 130 m to nearly 18 km. This study classified 35 of these circulations as tornadoes using a series of tests that weighed track characteristics and radar data. Unusual features, such as a likely tornado merger and multiple instances of tornadoes occluding behind the leading edge of the QLCS surface cold pool, are examined. Possible genesis mechanisms and National Weather Service operational implications are also discussed. A new, behavioral-based approach for identifying a tornadic debris signature (TDS) is presented that may be better suited for QLCS tornadoes. Twelve TDSs were cataloged on 31 August 2014 using this methodology at ranges up to 90 km from the Des Moines, Iowa, WSR-88D.

1. Introduction

Aerial surveying has been an integral component of tornado research and National Weather Service (NWS) storm surveys since the middle of the twentieth century (Van Tassel 1955; Fujita et al. 1970; NWS 2011; Karstens et al. 2013; Wakimoto et al. 2016), with Fujita in particular leveraging over 300 airborne surveys throughout his storied career (McDonald 2001). Tornado track assessments via high-resolution satellite imagery began in the late 1990s (Yuan et al. 2002; Jedlovec et al. 2006) and continue to this day, with current publicly available imagery oftentimes ≤1 m in resolution at nadir (Burgess et al. 2014; Satellite Imaging Corporation 2016). The first documented case of the NWS using satellite imagery to augment a traditional ground survey took place following the 27 April 2011 tornado outbreak across the southeastern United States (Molthan et al. 2014). On-demand satellite imagery is now available for NWS Weather Forecast Offices (WFOs) to request following natural disasters to aid in partner response

and historical documentation (Skow 2014; Schultz et al. 2016).

However, aerial and satellite-based photography is oftentimes reserved for high-impact tornadoes or the comparatively few events sampled by field research teams (e.g., Fujita et al. 1970; Fujita 1974; Atkins et al. 2005; Molthan et al. 2014; Wakimoto et al. 2016). According to the National Oceanic and Atmospheric Administration/National Centers for Environmental Information (NOAA/NCEI) Storm Events Database (NCEI 2016), the vast majority (80%) of U.S. tornadoes documented since 1950 have been low impact—category 0 or 1 on the Fujita (F) and enhanced Fujita (EF) scales (Fujita 1981; Edwards et al. 2013)—and seldom studied to such fine degrees of detail. When broken down by convective mode, over 75% of documented tornadoes occur with cellular convection with less than 20% cataloged with quasi-linear convective systems (QLCSs; Trapp et al. 2005). Trapp et al. (2005) subdivided QLCS tornadoes furthermore by F-scale category and diurnal occurrence, confirming that QLCS tornadoes have a tendency to be both weaker than their discrete counterparts and develop during the late evening and
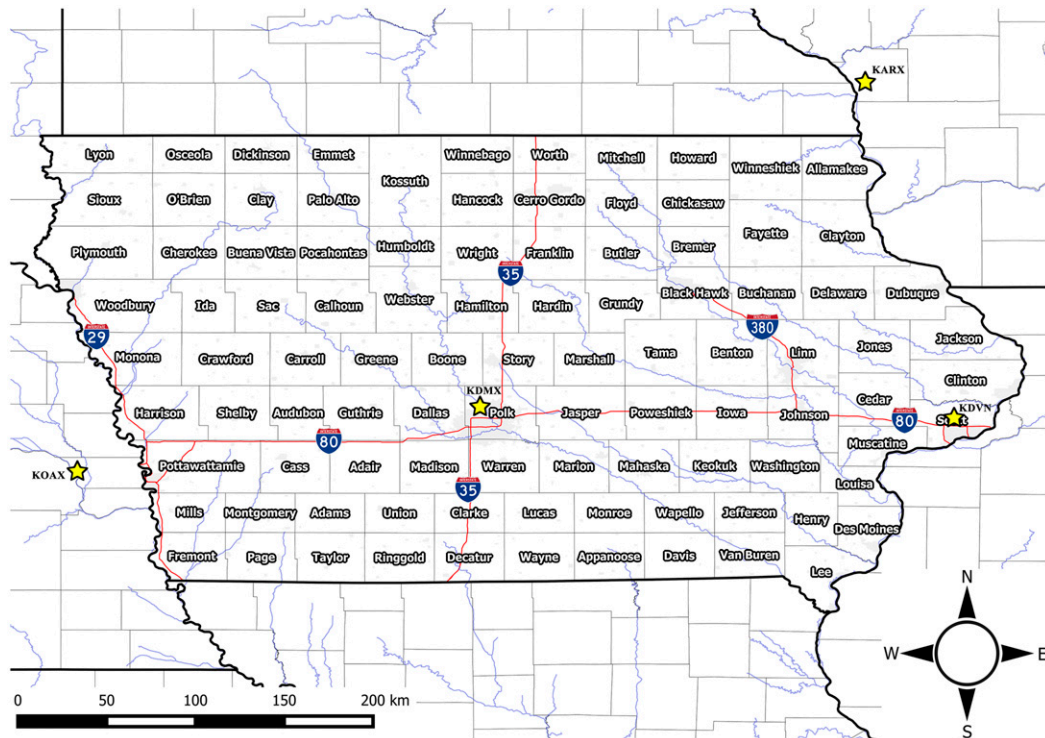
FIG. 1. Reference map of the state of IA with county names/outlines, urban boundaries (light-gray filled), interstate highways (red), and rivers (light blue) overlaid. Yellow stars indicate the KDMX, KOAX, KARX, and KDVN WSR-88D site locations. All track and aerial imagery figures (with the exception of Fig. 14) are cylindrical map projections while radar images and Fig. 14 are azimuthal equidistant projections centered on the respective radar sites. All maps and radar data use the World Geodetic System 1984 [European Petroleum Survey Group (EPSG:4326)] datum and are aligned to true north.

overnight hours. Consequently, the number of aerial-based QLCS tornado studies is limited (Forbes and Wakimoto 1983; Wakimoto 1983; Atkins et al. 2005). The detailed airborne survey by Forbes and Wakimoto (1983, hereafter FW83) following the 6 August 1977 bow echo over central Illinois revealed an intense concentration of 18 tornadoes within a 20 km × 40 km area, two of which produced F2 and F3 damage.

Despite the lack of aerial studies, the meteorological community has made great strides on multiple facets related to QLCS tornado research, enabling forecasters to determine environments and possible mechanisms conducive for their genesis (Schaumann and Przybylinski 2012; Schenkman and Xue 2016). Nonetheless, operational QLCS tornado forecasting and real-time/poststorm verification remains extremely challenging (Brotzge et al. 2013). Social media has improved the documentation of these short-lived and narrow tornadoes, but many take place over rural country and fail to impact ratable damage indicators. These tornadoes are sometimes embedded in straight-line winds that produce similar degrees of damage, making ground-based distinctions between meteorological damage sources difficult. NWS ground surveys, generally limited by available road networks and office staffing, may not be deployed if little to no damage is reported to a WFO.

Following the passage of a QLCS on the evening of 31 August 2014 (the event hereafter referred to as 31A14) through the state of Iowa (see Fig. 1 for reference map), the entire state was photographed by happenstance during an annual agricultural aerial survey. As in FW83, the mature agricultural land cover of the region provided an excellent medium on which to document storm-scale wind phenomena. We examine the findings of this aerial analysis in combination with the superresolution (0.25 km × 0.5° range gate) (Torres and Curtis 2007), polarimetric, and improved low-level temporal scanning strategy updates now available with NWS Weather Surveillance Radar-1988 Doppler (WSR-88D) data. Based on this analysis, we propose both an empirical probabilistic track classification scale and a new behavioral-based tornadic debris signature (TDS) identification scheme. We revisit some of the same questions and genesis theories posed by FW83,

incorporating the scientific and technological advances that have transpired in the ensuing three decades using a high-resolution, twenty-first-century dataset.

2. Data and methodology

a. Radar and environmental data

Polarimetric, superresolution level II radar base moments from the Des Moines, Iowa (KDMX); Omaha, Nebraska (KOAX); La Crosse, Wisconsin (KARX); and Davenport, Iowa (KDVN) WSR-88Ds were interrogated through the Gibson Ridge Level II Analyst (v. 2.50) radar-viewing application (http://www.grlevelx.com). All four radar sites were running in volume coverage pattern (VCP) 212 for the duration of the event with the Supplemental Adaptive Intra-Volume Low-Level Scan (SAILS) option enabled, providing an additional 0.5°-elevation scan midway through the VCP (ROC 2012). Maximum 0.5° rotational velocity [$V_{rot} = (|V_{in}| + |V_{out}|)/2$] values during the lifespan of a damage path were only calculated for discrete, subjectively resolved, (superresolution) gate-to-gate storm-relative velocity (SRV) rotational couplets with ≤45° separation angle—the size of a tornadic vortex signature (TVS; Brown et al. 1978; Brown and Wood 2012). Since the vortices were not associated with supercellular mesocyclones and rarely exceeded the aforementioned size attributes, V_{rot} was calculated in this manner. There was no minimum V_{rot} for defining a couplet in this study since their discernibility was a function of both V_{rot} strength and the azimuthal shear across the QLCS convergence zone in which they were frequently located, in addition to the distance from a WSR-88D. Temporal SRV trends helped assess the presence of a couplet. The constructed damage tracks (discussed in section 2c) were superimposed upon radar data to derive best-estimate start and end times, either by matching the track to a couplet, spectrum width σ_v maximum (Lemon 1999; Spoden et al. 2012), or the leading edge of the cold pool (Weisman and Trapp 2003, hereafter WT03) as resolved by radial velocity V_r. KDMX executed a performance check at the end of the 0120 UTC volume scan, resulting in a ~2.5-min delay before the start of the 0128 UTC volume scan. Level II data were corrupted for the 0128 UTC volume scan, which necessitated the substitution of level III data for the radar analysis, for which SAILS data were unavailable.

Determining how to best identify nonmeteorological scatterers being lofted into a polarimetric radar sample volume by a tornado, also known as a TDS (Zrnić and Ryzhkov 1999; Ryzhkov et al. 2005, hereafter R05), remains an unresolved matter in the meteorological community. Collocated product-based thresholds of horizontal reflectivity Z_{HH}, V_r/SRV, copolar cross-correlation coefficient ρ_{hv}, and differential reflectivity have been in use since the TDS was first defined (R05), but have differed between various studies and sources (e.g., R05; Schultz et al. 2012; Bodine et al. 2013; Van Den Broeke and Jauernic 2014, hereafter VJ14; WDTD 2016). Van Den Broeke (2015) expressed that "specific thresholds of the polarimetric variables have proven challenging to define," depending on factors such as the extent of the precipitation entrainment and variations in land cover.

Based upon the authors' experience with this and similar cases, we propose a new method for determining the presence of a TDS in WSR-88D polarimetric data that relies on the behavioral trends of a ρ_{hv} minimum (hereafter ρ_{hv}–min) collocated with a V_r/SRV rotational couplet or convergence zone and in a region of adequate signal quality, meeting the lower-bound Z_{HH} criteria of ≥20 dBZ proposed by VJ14. In this study, there is no set upper-bound ρ_{hv} value; instead, the ρ_{hv}–min should be composed of at least four contiguous superresolution range gates in a semicircular orientation. These range gates should all have a difference of ≥0.03 compared to the ambient ρ_{hv} data field and at least one pixel in the TDS containing a difference of ≥0.05 compared to this same field. This ρ_{hv}–min should originate at the 0.5°-elevation tilt or, in some rare cases, the 0.9°-elevation tilt if the 0.5° scan completes just prior to the onset of debris lofting. However, the ρ_{hv}–min should be present at the 0.5° tilt at some point during the lifespan of the TDS. The 0.5° ρ_{hv}–min must persist for at least two scans (SAILS inclusive) or be present between the 0.5° and at least the 0.9° tilts in a single volume scan to be counted as a TDS using our classification scheme. In nearly all instances analyzed in this and other case studies, the diameter of the 0.5° ρ_{hv}–min increases with time, akin to a plume (see Figs. 2a–d for an example). The height of the ρ_{hv}–min tends to increase with time while the tornado is in progress, but can vary depending on the types of debris lofted, precipitation loading, and tornado strength (VJ14; Entremont and Lamb 2015; Van Den Broeke 2015). As with product-based methods, one should be alert for ρ_{hv} signatures that may appear similar to those produced by a tornado, especially nonmeteorological debris being ingested into a thunderstorm updraft. Ensuring that the ρ_{hv}–min is tied to a V_r couplet or convergence zone and exceeds the Z_{HH} lower-bound criteria greatly reduces these false positives. It may be difficult to discern small TDSs along QLCS convergence zones characterized by a long, narrow ribbon of reduced ρ_{hv}. In such instances, our experience shows that examining the vertical continuity in the ρ_{hv}–min helps in discerning the presence of a TDS.
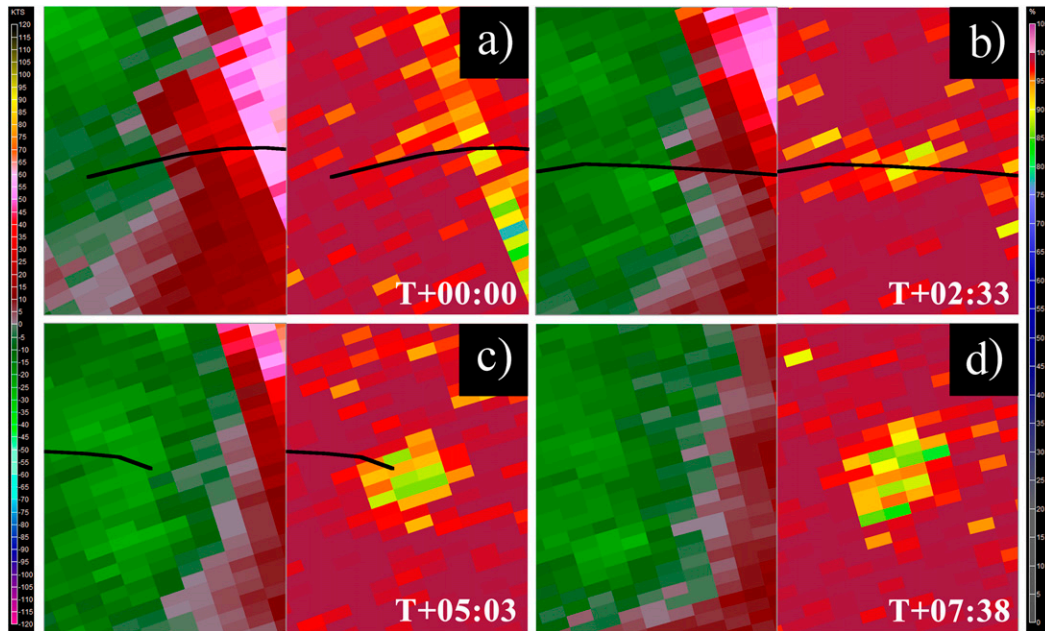
FIG. 2. Feature-following two-panel time sequence of 0.5° (left) SRV and (right) ρ_{hv} showing the evolution of a 31A14 TDS with a weak couplet but distinct, temporally expanding ρ_{hv}–min at a range of 69 km from KDMX (height of 850 m). The path of the tornado (56-T17) is denoted by a black line [note that the end of the tornado track is outside of the viewing area on the last pane in (d)]. All V_r, SRV, and σ_v product units in the study figures are in knots (kt, where 1 kt = 0.5144 m s^{-1}). Each pixel in this and all subsequent radar images represents one super-resolution range gate. The user-defined storm-relative motion (SRM) was set to 273° at 43 kt (22.1 m s^{-1}). (a) Starting at 0135:57 UTC ($T + 00{:}00$, SAILS), the tornado is in progress with no definable couplet or TDS. (b) By 0138:30 UTC ($T + 02{:}33$), a couplet with a V_{rot} of 18.5 kt (9.5 m s^{-1}) is discernable along with a 1.74-km^2 ρ_{hv} depression containing a minimum value of 0.89. (c) At 0141:02 UTC ($T + 05{:}03$, SAILS), the tornado and couplet have dissipated and the ρ_{hv} depression area has expanded to 3.02 km^2 with a minimum value of 0.86. (d) The TDS areal coverage continues to expand to 4.59 km^2 at 0143:35 UTC ($T + 07{:}38$) and minimum values fall to 0.82. The TDS rapidly decays by 0146:09 UTC ($T + 10{:}12$, not shown).

This process differs from cited studies/sources by 1) removing the strict dependency of ρ_{hv} criteria and 2) acknowledging that tornadogenesis can occur with certain storm modes and environments, which results in shallow or compact circulations (such as QLCSs) that can prove challenging for radar operators to resolve, necessitating the inclusion of convergence zones in the V_r analysis. It is a scalable technique that identifies the physical debris-lofting processes taking place—processes that should become easier to recognize with the newly implemented Multiple Elevation Scan Option for SAILS (MESO-SAILS) WSR-88D upgrade installed earlier in 2016 (ROC 2014), reducing the 0.5°-elevation tilt update times to 1–2 min. The utility of this technique was demonstrated in preliminary work by the first author using five additional low-topped convection, QLCS, and landspout case studies in central Iowa during 2014 and 2015 (Skow 2015, 2016). Each case contained at least two TDSs with either weak or unresolvable V_r rotational couplets that were identified using the criteria proposed in this study. In three of the five cases, no

visual reports of tornadoes were received by the NWS. Thorough ground and aerial surveying following each case revealed narrow, convergent damage paths with each TDS if all modes of surveying were leveraged and ground cover permitted the identification of a path (see section 2b for ground cover discussion). More information on the TDSs associated with 31A14 can be found in section 4a.

Prestorm environmental data were obtained through a subjective analysis of contoured images provided by the NOAA/NWS/Storm Prediction Center's hourly mesoanalysis (Bothwell et al. 2002) website (http://www.spc.noaa.gov/exper/mesoanalysis/).

b. Aerial imagery

The four-band (red, green, blue, and near-infrared) ~1-m ground sample distance imagery used for this study was obtained through the National Agriculture Imagery Program (NAIP), a U.S. Department of Agriculture (USDA) Farm Service Agency that captures aerial photos throughout the continental United States
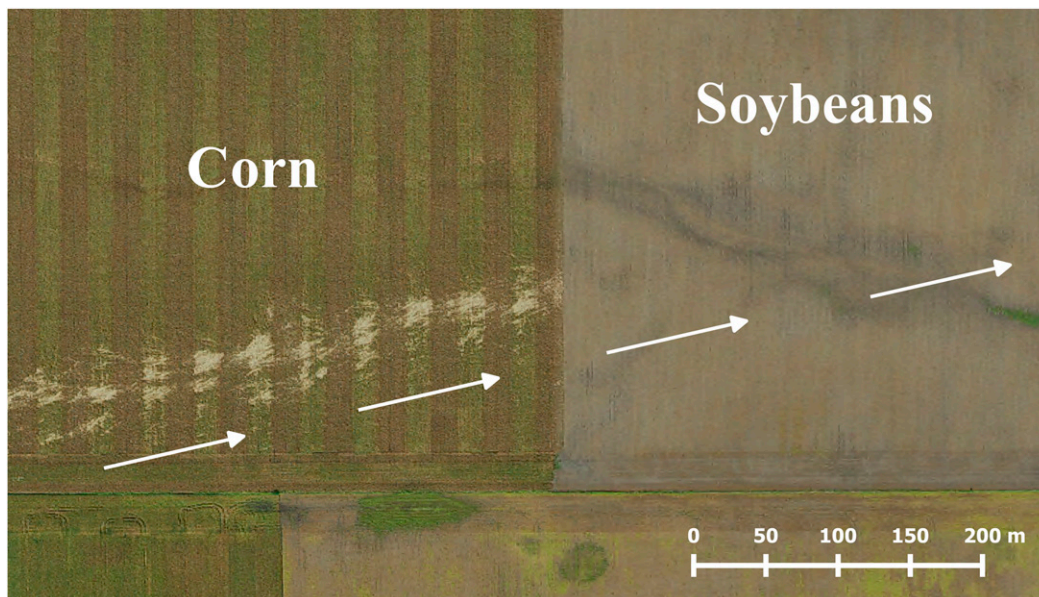
FIG. 3. Tornado 56-T17 highlights how crop type and different crop hybrids affected the visibility of the 31A14 damage paths in the aerial imagery. A corn field is shown along the left side of the photo and a soybean field on the right. Note the variations in damage between the two corn varieties planted (identifiable by the different row colors). This photograph was taken on 22 Sep 2014. Arrows under the path indicate path direction to the east-northeast.

once per growing season (USDA 2015). The 2014 Iowa NAIP dataset was collected on nine dates between 6 September and 15 October and made available in early 2015. County-based, mosaicked Geographic Information System raster files were downloaded from the USDA Geospatial Data Gateway (https://gdg.sc.egov.usda.gov/GDGOrder.aspx) and composed in QGIS (http://www.qgis.org/). Multiple online mapping services containing these photos as a tiled layer were also employed, including the NWS Damage Assessment Toolkit (DAT; Camp et al. 2010; Burgess et al. 2014; Camp et al. 2014). The aerial imagery was manually scrutinized for crop, tree, or structural damage. Crop harvesting degraded the utility of the imagery captured during the month of October; however, this only affected a small subset of the sample area, primarily in Carroll and Hardin Counties. Crop type and even the specific hybrid of a given crop type played a large role in the visibility of damage swaths. Corn and soybean fields were the two forms of agricultural land types impacted by this event. The high-profile, mature cornfields were the ideal medium for assessing wind patterns with the greatest degree of detail (FW83). Soybeans, with their shorter, thinner, and more flexible stalks, were less susceptible to disruption identifiable in the aerial photos. As a result, damage tracks oftentimes appeared to "skip" over soybean fields (Fig. 3).

The imagery resolution was not suitable for determining individual crop-fall patterns; consequently, a sample area approximately 10–15 m or greater in width was required to estimate wind trajectories. The narrowest damage swaths oftentimes fell under this threshold, making crop-fall pattern determinations problematic. Tree damage proved difficult to locate without preexisting upstream or downstream crop damage and was limited to a few shelterbelts and river valleys. In nearly all instances, the resolution of the photos was sufficient to distinguish between meteorological damage and natural or anthropogenic features, including but not limited to ridgelines, streambeds, trails, washouts, and buried utility lines. In cases of ambiguity, the feature in question was evaluated against imagery from previous years to determine its source.

For the purpose of this study, the words track and path pertain to a nondiffluent region of damage with a length-to-width ratio ≥ 4:1. Other descriptive words such as swath and damage, unless otherwise defined, refer to wind fields of all characteristics. A battery of tests was conducted to ensure that the observed damage was from 31A14:

1) Two ground-surveyed tornado tracks and four areas of wind damage (see section 3) were matched to the NAIP data.
2) Reports and photos from 31A14 were researched and fitted to the corresponding damage swaths.

Test 1: Damage Patterns
Purely Diffluent Flow [1] ✔ → Downburst

Test 2: Likely Tornado Qualities
Tornadic Debris Signature [2] or
Tree/Structural Damage [3] ✔ → Tornado

Test 3: Path Characteristics
Short & Intense Damage Path [4] or
Long & Moderate Damage Path [5] ✔ → Tornado

Test 4: 10-Point Ranking System to Classify Path

Points	Criteria
(1-3)	Crop damage: Tier I (1 pt), II (2 pts), or III (3 pts) [6]
(3)	Swirl ratio of at least a one-cell vortex [7]
(1-2)	Track length > 1.5 km (1 pt), > 3 km (2 pts)
(1)	Circulation not embedded in downburst [8]
(1)	Rotational couplet [9]
(+/- 2)	Extenuating circumstances [10]

Misovortex — Unknown — Tornado
0 - 3 | 4 - 6 | 7 - 10
Cumulative Point Score

[1] Flow patterns resolved using the mean crop-fall patterns and damage intensity. Linear (neither confluent or diffluent) patterns or narrow damage areas (generally <15 m in width) in which the crop-fall patterns could not be resolved were counted as tracks.

[2] TDSs identified using the technique outlined in Section 2a.

[3] Aerial imagery also compared to pre-event imagery to determine areas of cleaned-up damage. Test fails if there is ambiguity to the meteorological source of damage.

[4] Track length of at least 2.5 km & continuous Tier III crop damage (Fig. 5c) for ≥0.75 km.

[5] Track length of at least 5.0 km & continuous Tier II crop damage (Fig. 5b) for ≥1.50 km.

[6] Crop damage of a given tier (see Figs. 5a–c for examples) must occur for a minimum cumulative distance of 0.50 km or 75% of the track length (whichever is reached first) to count.

[7] Continuous for at least 0.50 km. If any ambiguity, set to 0. See Section 2c for more information.

[8] At peak tornado intensity. Downbursts were often observed at the beginning or end of a track.

[9] Subjectively-resolved in SRV using the processes outlined in Section 2a.

[10] May include: environment, location within storm, track behavior, upstream/downstream track types, cropland character etc. Up to a +/- 2 point swing (cannot go beyond scale limits).

FIG. 4. Flowchart detailing the testing and binning scheme used to catalog 31A14 tracks.

3) The damage swaths were cross-referenced against couplets, TDSs, and the overall Z_{HH} and V_r QLCS storm structure.

4) Using the NAIP data, tornado tracks from other central Iowa events earlier in 2014 were vetted against the known 31A14 paths to develop a rudimentary understanding of agricultural damage track aging. Damage tracks from nine tornado events in May and June could not be found in the aerial data owing to the lack of mature crops during this time frame. Multiple EF0/EF1 tornado tracks from 6 July (Grundy/Tama Counties) and 17 August (Emmet County) were located. On-demand, high-resolution satellite imagery (Skow 2014; Schultz et al. 2016) taken 3 days after the 6 July tornadoes were compared with the NAIP photographs taken in September. These tracks experienced considerable vegetation recovery in the intervening 2 months and were difficult to locate on the NAIP imagery. The 17 August and (ground surveyed) 31A14 damage paths showed little to no cropland recovery. Three previously undocumented tracks from events earlier than 31A14 were discovered using this technique.

5) Storm reports and radar data in the August and September 2014 time frame were investigated to see if any of the damage could have originated from a different storm. A narrow 14-km-long tornado path and nearby microburst first discovered via the aerial data in Dallas County were determined to have occurred on 9 September and were eliminated from the analysis. Multiple rounds of convection did impact the study area during the late summer months, making a confident event source determination difficult in cases where the damage areas were displaced $\sim \geq 100$ km from a WSR-88D. Nevertheless, the strong correlation of track locations to the apexes and northern elements of the convective bowing segments (FW83; Rotunno et al. 1988; Przybylinski 1995; Funk et al. 1999; WT03; Atkins and St. Laurent 2009a), the nearly unidirectional east-to-northeastward track headings orthogonal to the convective line orientation, and the lack of damage outside of these narrow corridors traversed by other storms that impacted the study area support our 31A14 causation argument.

c. Cataloging the damage swaths

The DAT was used to construct damage polygons and best-fit lines for each discrete path. Multiple tracks along
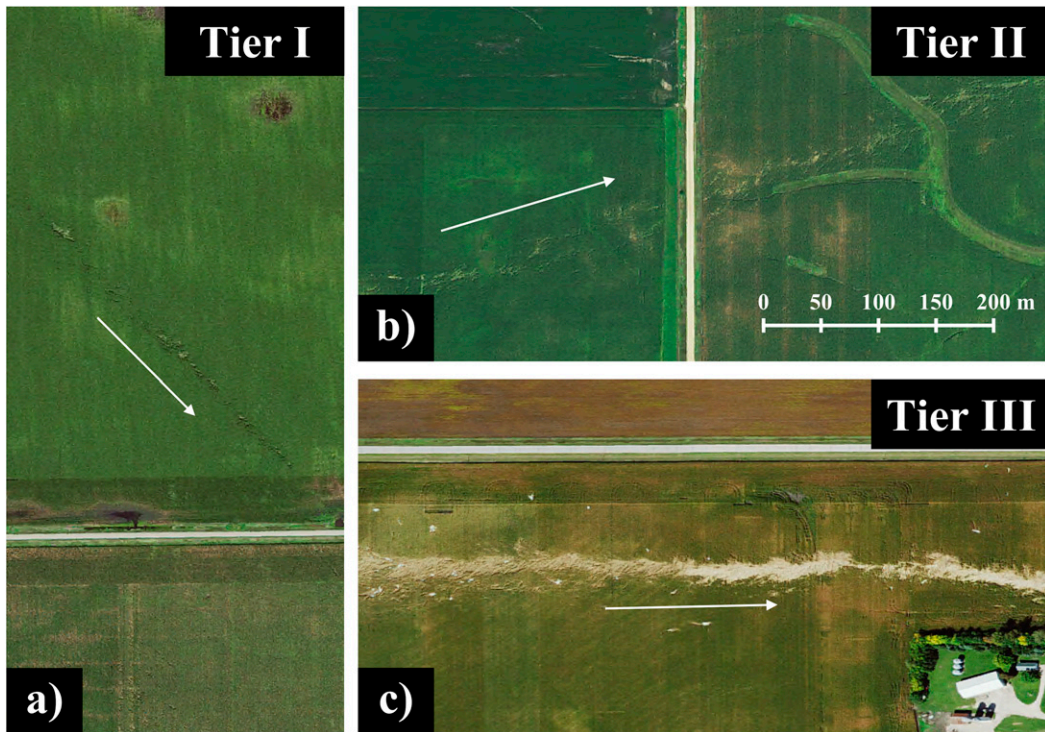
FIG. 5. Examples from 31A14 of the three tiers of crop damage used to assess damage paths. All images are rendered to the same scale and arrows indicate direction of travel. The following are text descriptions of the three tiers. (a) Tier 1: a narrow (generally <20 m) or very intermittent path in corn. Also encompasses tracks whose convergent patterns are not resolvable due to their narrow path width. Will not show in soybean fields. (b) Tier II: longer streaks of semicontinuous/continuous damage in corn with wider tracks (generally >20 m). Faint markings in soybean fields possible. (c) Tier III: a solid, continuous path of downed corn at least 20 m across (total track width oftentimes wider) and/or a continuous path in soybean fields.

the same heading within 1 km of another were classified as a single, intermittent track, taking into account instances when the track may not be visible because of the land cover type. FW83 classified all nonmechanically-induced vortices as tornadoes regardless of path characteristics. Our study went a step further and developed an empirical classification procedure to establish the likelihood that a given circulation was tornadic using multiple track characteristic and radar data inputs. The flowchart in Fig. 4 provides additional details to supplement the following procedural summary.

First, it was determined whether the wind field in question was purely diffluent based on the intensity, continuity, length-to-width ratio, and mean crop-fall patterns of the damage swath. Narrow wind swaths that were convergent, exhibited neither confluence nor diffluence, or were too narrow to resolve crop-fall patterns were forwarded on to successive tests. Next, all paths with TDSs or structural/tree damage were deemed a tornado (a side note: if one bypassed the

TDS test, all of the affected tracks would have still been classified as tornadoes using the path characteristic and damage tests covered later in this paragraph). Comparing the NAIP data with earlier aerial imagery permitted for the identification of structural/tree damage areas, some of which had already been removed but were identifiable through freshly disturbed earth. Observed structural/tree damage in the aerial data was discounted in instances where straight-line winds were coincident with damage paths and may have factored into causing the damage. Tracks failing the previous test underwent a combined pathlength and crop damage assessment. Both variables were binned into three tiers, and tracks exceeding two different combinations of crop damage and length characteristics were labeled as tornadoes (see Figs. 5a–c for crop damage tier examples). This is similar to the Fujita–Pearson scale (Fujita and Pearson 1973), which ranks tornadoes based on damage (F scale) along with pathlength and width. This same philosophy was employed here to determine the probability of a damage
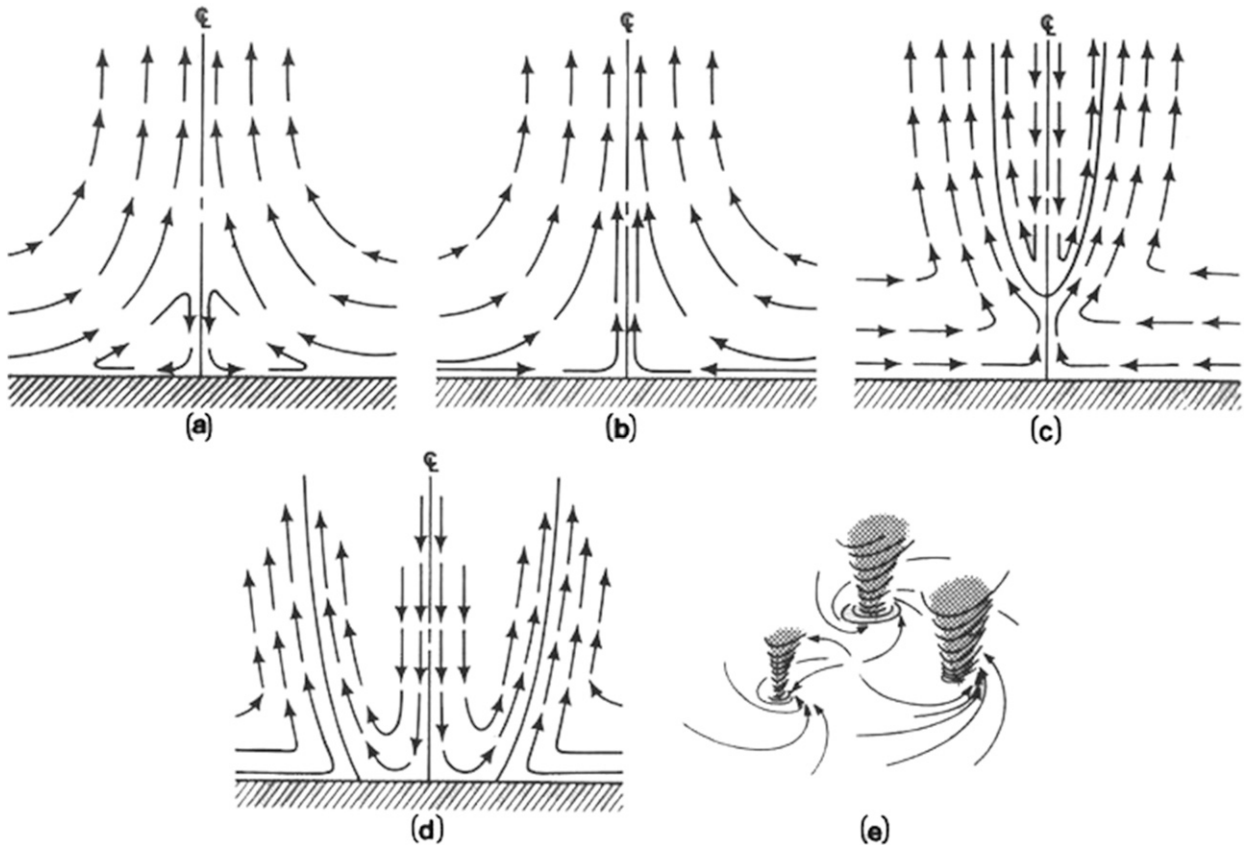
FIG. 6. Conceptual model of a tornado vortex structure at progressively higher swirls ratios from Davies-Jones (1986). (a) Boundary layer flow separates and passes around the corner region. (b) One-cell vortex. (c) Vortex breakdown due to a descending downdraft. (d) Two-cell vortex with downdraft impinging on the ground. (e) Multiple vortex structure. (Used with permission from the University of Oklahoma Press.)

track being tornadic. The remaining unclassified paths were ranked on a 10-point scale, which primarily weighed path characteristics. Based on the sum of these points, the tracks were binned into one of three groups: ''misovortex,'' ''unknown,'' and ''tornado.'' Under rare circumstances, owing to the fact that a completely objective classification technique was unfeasible to develop, the score could be adjusted by up to ±2 points (see Fig. 4 for potential rationales). The reasons for each adjustment were carefully documented and the impact on the final statistics is presented in section 4a.

Several aspects of the final scoring system are discussed below. In addition to track length and crop damage, the subjectively analyzed track swirl ratio (Davies-Jones 1986, hereafter D86) was factored into the score. Multiple long and narrow tracks were observed that exhibited either a linear wind field or weak convergence at best. In these situations, the swirl ratio was felt to be the best scientific discriminator for

taking into account these flow patterns. The swirl ratio S can be defined as

$$S = \frac{r_0 \Gamma}{2Qh}, \qquad (1)$$

where r_0 is the radius of the updraft, Γ is the circulation at r_0, Q is the volume flow rate across the updraft, and h is the inflow depth (Church et al. 1979; Snow et al. 1980). With very low values of swirl ratio, the flow is dominated by the updraft instead of rotation; a surface air parcel with a lateral trajectory into the vortex experiences ascent before reaching the centerline of the vortex, also known as the corner region, and no concentrated vortex appears at the surface. As S increases, the surface flow penetrates to the center of the vortex before experiencing lift and is referred to as a one-celled vortex. As S grows larger, the vortex widens as a centralized downdraft forms aloft, eventually reaching the surface and forming a two-celled and ultimately multivortex structure (Lewellen 1993). Most swirl ratio studies to this point have been idealized
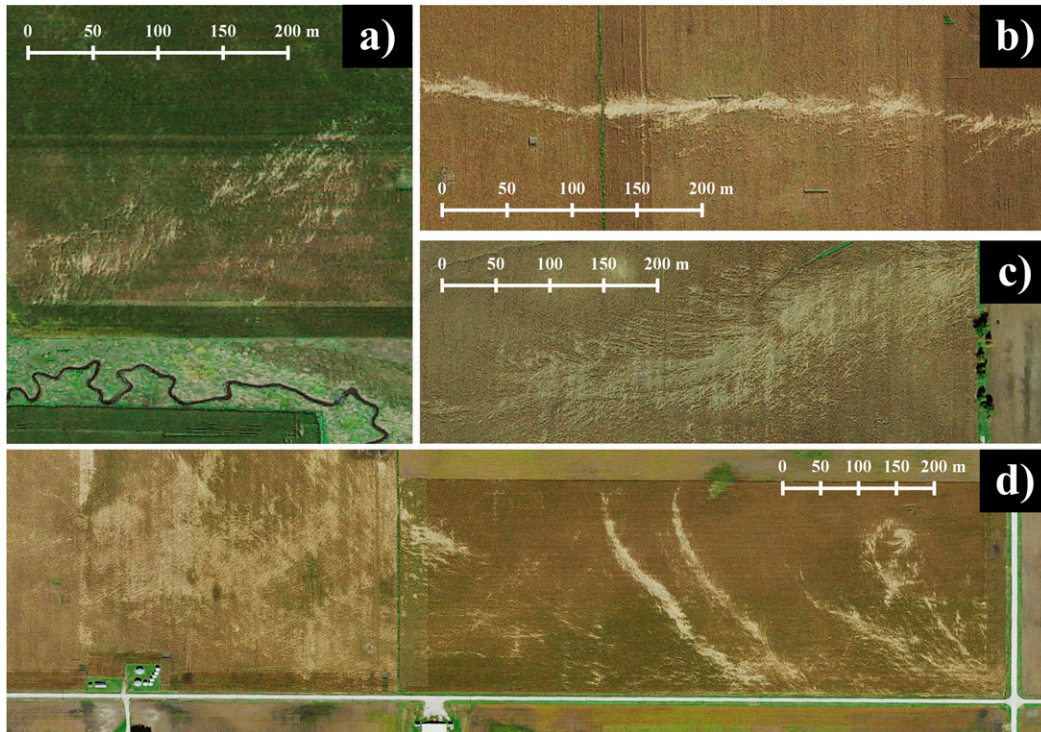
FIG. 7. Examples of hypothesized, successively higher swirl ratios from 31A14 aerial imagery as derived from Fig. 6 with corresponding tracks denoted in parentheses. (a) As in Fig. 6a (24-U4). (b) As in Fig. 6b (56-T17). (c) As in Figs. 6c and 6d (16-T9). (d) As in Fig. 6e (54-T16). Note the stark difference between the linear, but narrow, flow pattern markings of (a) and the tight convergence of (b).

laboratory experiments or numerical simulations (Church et al. 1979; Snow et al. 1980; Lewellen et al. 2000; Karstens et al. 2010). No observational studies could be found that provide visual aerial depictions of different values of *S*, likely owing to additional factors such as horizontal translation, larger-scale environmental winds, and friction influencing the observed surface wind field characteristics (Snow et al. 1980; Lewellen et al. 2000). Nonetheless, using the descriptions and graphic supplied by D86 (Figs. 6a–e), the physiognomy of each damage track was evaluated for evidence of a sustained swirl ratio equivalent to at least a one-cell vortex. Idealized examples from 31A14, both in terms of a homogenous agricultural land cover background and a circulation with minimal environmental wind contamination moving at a rate of speed slow enough to adequately resolve a swirl ratio, are presented in Figs. 7a–d. Given the $25\,\mathrm{m\,s^{-1}}$ storm motion and the possibility of tornadoes failing to leave a damage track strong enough to resolve a swirl ratio, a track with an incalculable swirl ratio could be classified as a tornado through other means. Conversely, owing to the possibility that nontornadic vortices could produce swirl ratio patterns similar to their tornadic counterparts, the swirl ratio was only one component of the classification scheme.

The term misovortex was used to describe paths with low scores, oftentimes owing to their short, weak tracks. This term utilizes the spatial wind-scale terminology proposed by Fujita (1981) for phenomena with diameters of 40–400 m. The classified 31A14 misovortices oftentimes had diameters that varied between the moso-α and miso-β subdivisions. However, given the likelihood of the wind field surrounding the vortices being slightly larger than the damage pattern would indicate, it was felt that the miso- prefix was more appropriate. The misovortex terminology is also a better description of the known qualities of the wind field, unlike the more common term of gustnado, which implies a ground circulation not connected to the cloud base. The available data could not conclusively determine whether a given track was separated from the cloud base. Conversely, a strong argument could be made for tracks of high tornadic probability, thus the use of the descriptor tornado in these instances.

An effort was made to assign all tornadoes an EF rating. Yet most either did not impact structures, had undergone too much damage removal to be ratable, or the imagery could not resolve the damage in enough detail to determine an accurate EF rating. An EF0 rating was
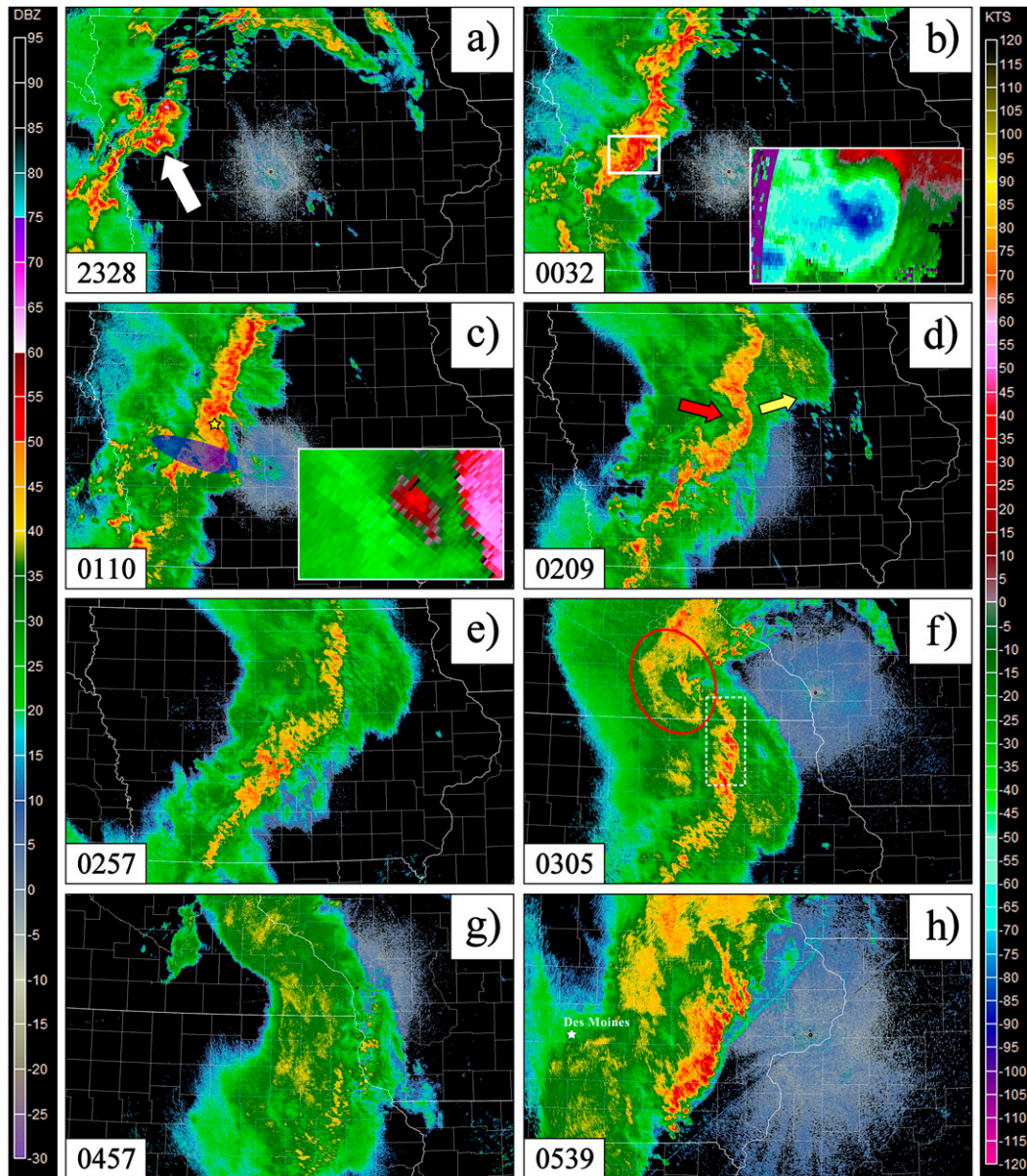
FIG. 8. The Z_{HH} (dBZ) time series of 31A14 from KDMX at (a) 2328, (b) 0032, (c) 0110, (d) 0209, and (e) 0257 UTC; from KARX at (f) 0305 and (g) 0457 UTC; and from KDVN at (h) 0539 UTC. The scale on the left is for Z_{HH} and the scale on the right is for both V_r and SRV imagery. The white arrow in (a) denotes the HP supercell prior to the line merger while the white square in (b) outlines the postmerger bowing line shown in the accompanying V_r insert. The semitransparent dark blue oval in (c) highlights the region affected by widespread damaging winds while the yellow star is placed upon the location of one meso-γ vortex shown in the SRV insert [SRM: 230° at 37 kt (19.0 m s^{-1})]. The red arrow in (d) corresponds to the developing RIJ, and the tan arrow ahead of the line denotes the propagation direction of the bow. The red oval in (f) encompasses the bookend vortex, and the dashed white rectangle is placed upon the bowing segment that briefly reintensified over northern IA.

assigned in these cases. Any downburst or inflow winds around a tornado were separated as best possible using the techniques and examples in Fujita (1978). All tracks were given a unique alphanumeric identification of xx-yzz, where xx is the chronologic order of the track, y is a single letter denoting the track class (T, tornado; U, unknown; and M, misovortex), and zz is the chronologic order of a particular track class.
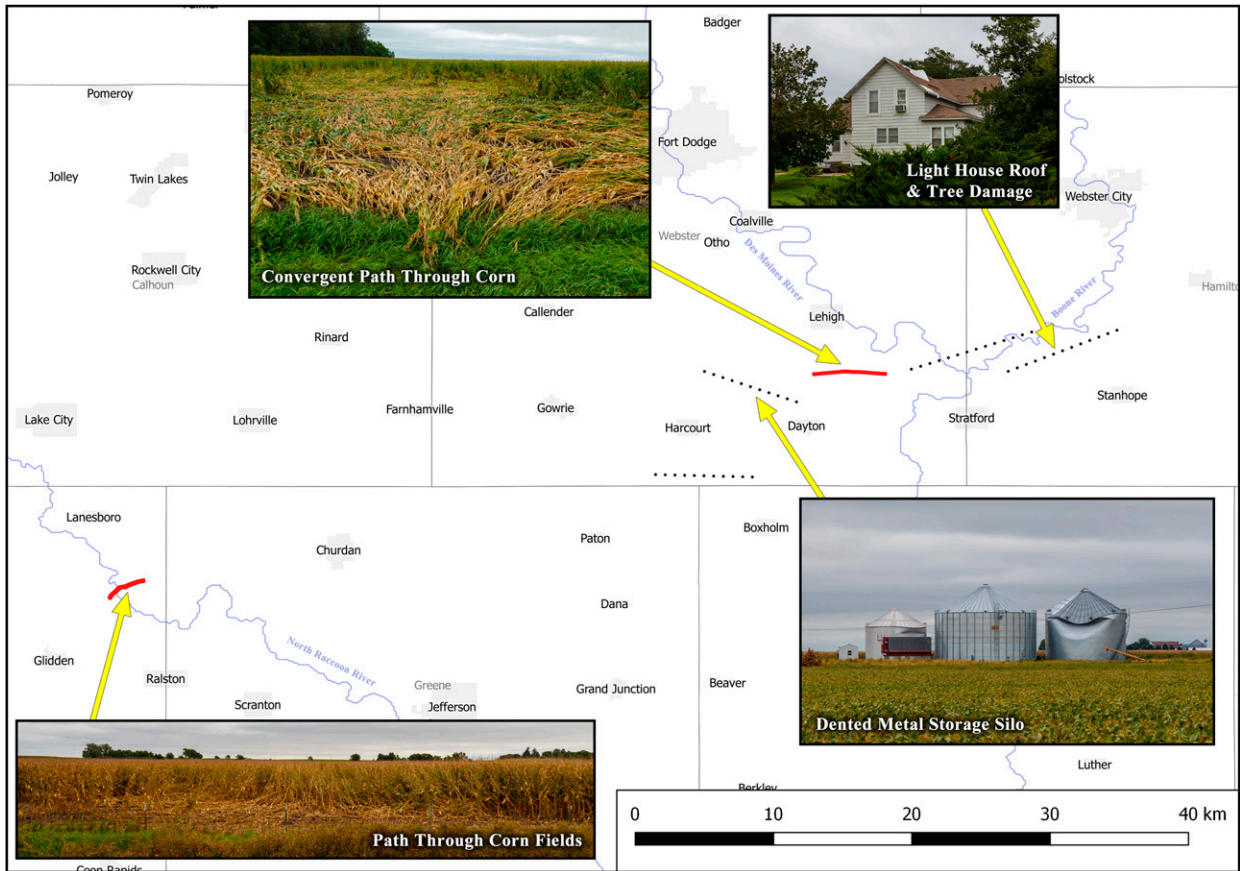
FIG. 9. The results of the ground survey conducted by the first author on 10 Sep 2014. Red lines represent tornado tracks and dotted black lines represent corridors of wind damage for which the meteorological source of the damage could not be determined. Example photos from four of the six locations surveyed are included with yellow arrows pointing to the location of the damage. County outlines and names, city outlines and names, and rivers are provided for background reference.

3. Event overview

The synoptic environment of 31A14 was characterized by a meridional upper-tropospheric short-wave trough digging southeast across Alberta, Canada, and the northern high plains with a 40–45 m s^{-1} 300-hPa jet located upstream over the western United States. At the surface, an eastward-advancing cold front extended south-southwest from a 998-hPa low centered along the Manitoba–North Dakota–Minnesota border to south-central Nebraska by 1800 UTC with temperatures and dewpoints in the warm sector of around 25°–30°C and 19°–22°C, respectively. Multiple, semidiscrete lines of convection developed across eastern Nebraska after 2100 UTC with a dozen 2.5–5.1-cm diameter hail reports received with these storms prior to 2300 UTC. Damaging winds became the predominant report type after 2300 UTC as the convection merged and crossed into western Iowa. The 2300 UTC prestorm environment

across central Iowa consisted of (the lowest 100 hPa) mixed layer convective available potential energy (MLCAPE) values of 2500–4000 J kg^{-1}, 0–6-km bulk shear values of 15–23 m s^{-1}, 0–1-km bulk-shear values of 10–18 m s^{-1}, effective storm-relative helicity indices of 300–400 m^2 s^{-2}, and mixed layer lifted condensation level heights between 750 and 1000 m AGL. These values fall well within the QLCS tornado environments defined by Thompson et al. (2012), with the notable exception of MLCAPE, which exceeded the 90th percentile of QLCS cases by 1000–1500 J kg^{-1}. The 2300 UTC surface analysis depicted an outflow boundary situated across central Iowa generated by early afternoon convection. This boundary lingered through 0000 UTC, but was no longer evident in observations after this time with winds veering from 90° to 140° and T/Td values experiencing an increase of 2°–3°C.

A high-precipitation (HP) supercell (Moller et al. 1994) developed between 2230 and 2330 UTC over
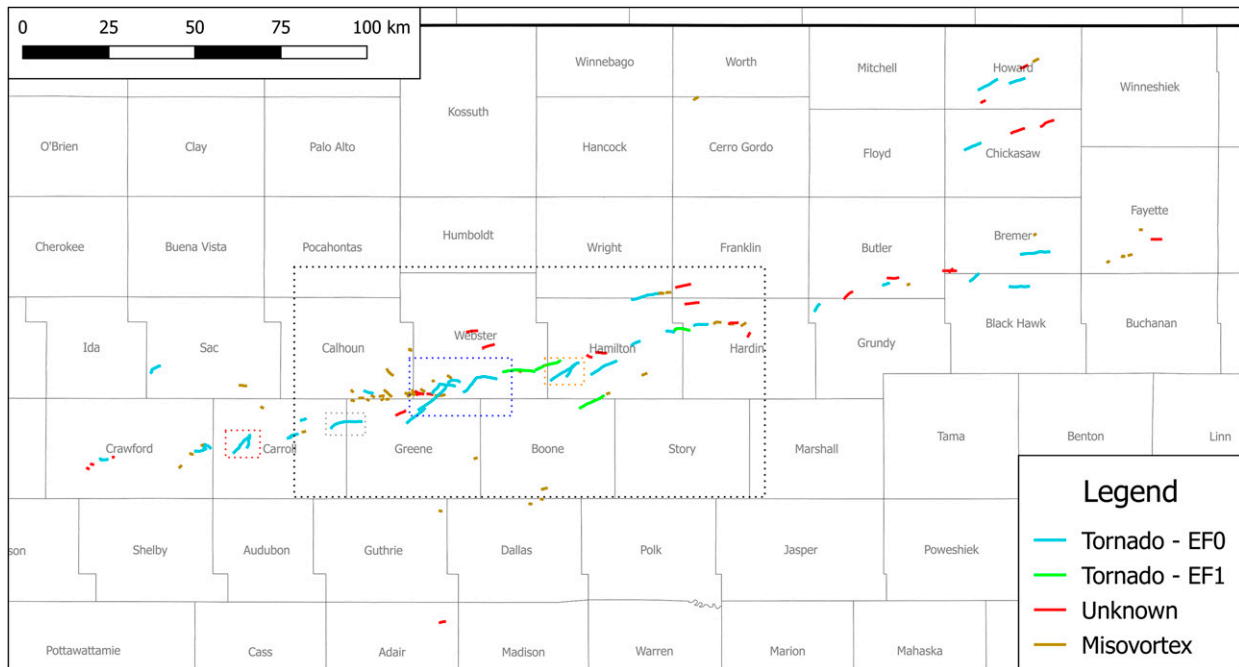
FIG. 10. Overview map of all cataloged tracks from 31A14 using best-fit track lines. Tracks are colorized by class and tornado EF scale (misovortex, brown; unknown, red; EF0 tornado, light blue; EF1 tornado, light green). Subset regions for subsequent maps are denoted by thin dotted lines (Fig. 14, black; Fig. 15a, orange; Fig. 16, red; Fig. 17, gray; Fig. 19, blue).

Monona and Crawford Counties in Iowa ahead of the approaching convective line (Fig. 8a). The merger of this nearly stationary supercell and convective line took place over Crawford County around 0000 UTC. The complex rapidly evolved into a bow echo (Fujita 1978) and by 0032 UTC (Fig. 8b) contained a 25-km-wide area of V_r values greater than $30 \, \mathrm{m \, s^{-1}}$ and a peak V_r of $48 \, \mathrm{m \, s^{-1}}$, as measured by KDMX at a beam centerline height of 1.8 km above radar level (ARL; hereafter, all radar-derived heights are measured from beam centerline ARL, assuming standard propagation). The bow echo accelerated eastward at speeds approaching $25 \, \mathrm{m \, s^{-1}}$ between 0015 and 0115 UTC, causing extensive wind damage from Crawford to Guthrie Counties. The northern segment of the bow elongated during this time (Fig. 8c) as a $30 \, \mathrm{m \, s^{-1}}$ rear-inflow jet (RIJ; Fujita 1978; Smull and Houze 1987) impinged on the line from the west-northwest. Two transient low-level meso-γ vortices (Orlanski 1975), analogous in some respects to a midlevel bookend vortex (Weisman 1990), developed on the north end of the bow between 0105 and 0130 UTC (Fig. 8c), where it bisected the trailing convective line that stretched to the Iowa–Minnesota border.

The bow reoriented itself on a northeastward heading after 0130 UTC (Fig. 8d) in conjunction with a strengthening RIJ (V_r of $39 \, \mathrm{m \, s^{-1}}$ as measured by

KOAX at a height of 3.5 km). The bow, after undergoing continued longitudinal expansion and upscale growth into a broader QLCS with multiple bowing segments, continued on its northeastward heading and showed a gradual weakening/cellular breakdown trend on V_r and Z_{HH} over the ensuing 3 h (Fig. 8e). A weak meso-β (Orlanski 1975) bookend vortex materialized along the north side of the QLCS over southern Minnesota around 0300 UTC (Fig. 8f), resulting in a brief reintensification of the bowing segment across Howard, Chickasaw, and Winneshiek Counties. The southern portion of the line developed a diffuse bowing signature east of Des Moines around 0330 UTC that cycled several times along and south of Interstate 80, producing sporadic severe wind reports along the way (Fig. 8h). The QLCS rapidly decayed as it crossed the Mississippi River between 0500 and 0730 UTC (Fig. 8g). While multiple areas of rotation had been noted by NWS meteorologists and two tornado warnings were issued during the event, no official storm survey was conducted by WFO Des Moines owing to the lack of serious damage reports the office received (SPC 2014).

On 10 September 2014, the first author conducted a personal ground survey of six subregions affected by the QLCS in Hamilton, Webster, and Carroll Counties (Fig. 9). Damage paths indicative of tornado strength
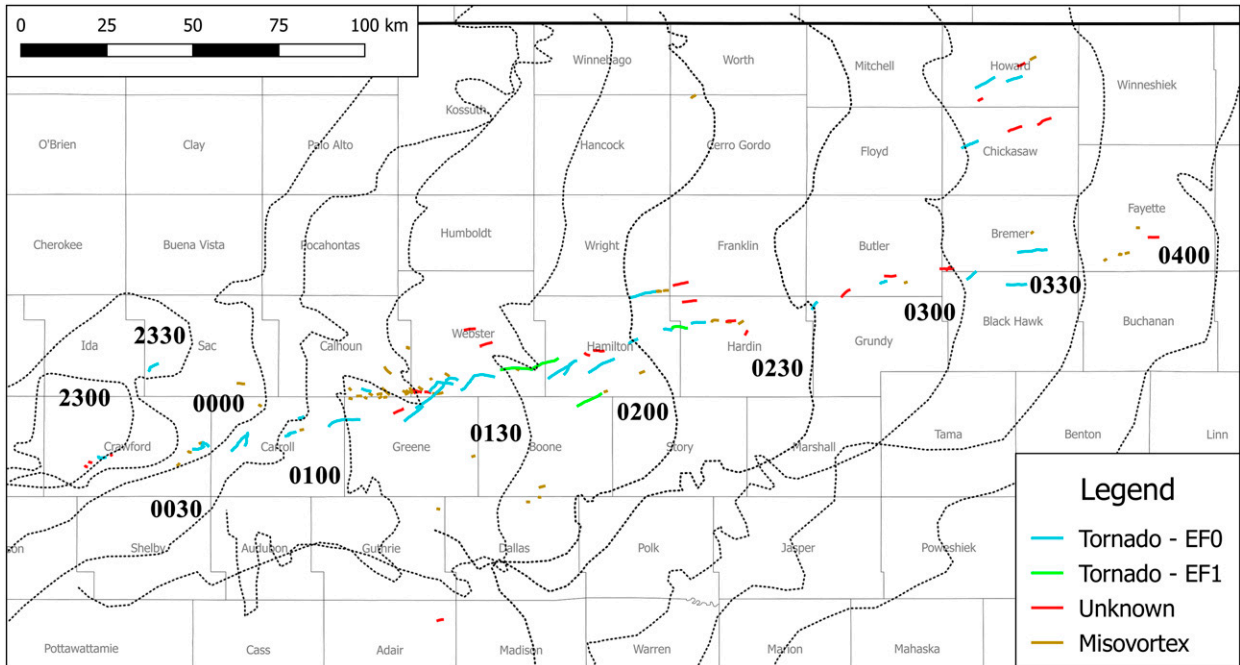
FIG. 11. As in Fig. 10 (minus additional figure coverages), but with the leading 40-dBZ Z_{HH} contour (black dotted lines) of 31A14 overlaid in 30-min intervals from 2300 to 0400 UTC as resolved by KDMX and KARX. Note the clustering of tracks along and north of the bowing apexes.

4. Results and noteworthy examples

a. Path and TDS statistics

circulations were found north of Dayton in Webster County and northeast of Glidden in Carroll County. The Webster County tornado left a pronounced 3-mi path through multiple fields and destroyed a hog confinement building, where damage was rated EF1. The 2-mi-long EF0 Carroll County tornado crossed the North Raccoon River, damaging small tree limbs, cornfields, and a small open livestock shelter. The survey found wind damage at the other four sites, but the meteorological source could not be established from the ground. Based upon the survey, two tornadoes were recorded in *Storm Data*. Aerial data discovered in late 2015 prompted a comprehensive reexamination of the event.

A total of 111 damage paths were cataloged from 31A14 and were classified as follows: 35 tornadoes, 25 unknown, and 51 misovortices. These tracks spanned a horizontal distance of 320 km across a 3.5-h window from 2322 to 0352 UTC. Pathlengths varied between 130 m and 17.61 km, with 38.7% < 1 km and 58.6% < 2 km in length. Sixteen tracks exceeded a length of 5 km. Over 90% of the 31A14 tracks exceeded a 10:1 length-to-width ratio. An overview path map is provided in Fig. 10, and details of each track are listed in the appendix. This includes five tracks from the HP supercell phase of the event and one small path along a boundary inflection point in Adair County. Nearly 85% of the damage paths fell within a 20–25-km-wide corridor along the northern segment of the main bowing convective line (Fig. 11). Thirty-one tornadoes were rated EF0, and four were rated EF1. An intense clustering of 22, mainly misovortex, tracks and downburst wind damage was observed coincident with the two aforementioned meso-γ vortices at the north end of the bow across a 28 km × 6 km area. The aerial data also resulted in the lengthening of both previously ground-surveyed tornadoes by a combined 9 km. Figure 12 provides examples of the different aerial track patterns. Scores were adjusted on 14 tracks owing to additional evidence not covered by the testing scheme outlined in Fig. 4. These adjustments resulted in two tracks being upgraded to "tornado" and another six to "unknown." For the other six times, the adjustment only moved the score to the upper or lower bound of a class and did not result in a class change.

Twelve TDSs were identified via KDMX data for 31A14 using the identification technique outlined in section 2a with examples provided in Figs. 13a–f. Eleven of these 12 TDSs were matched to ground tracks, with
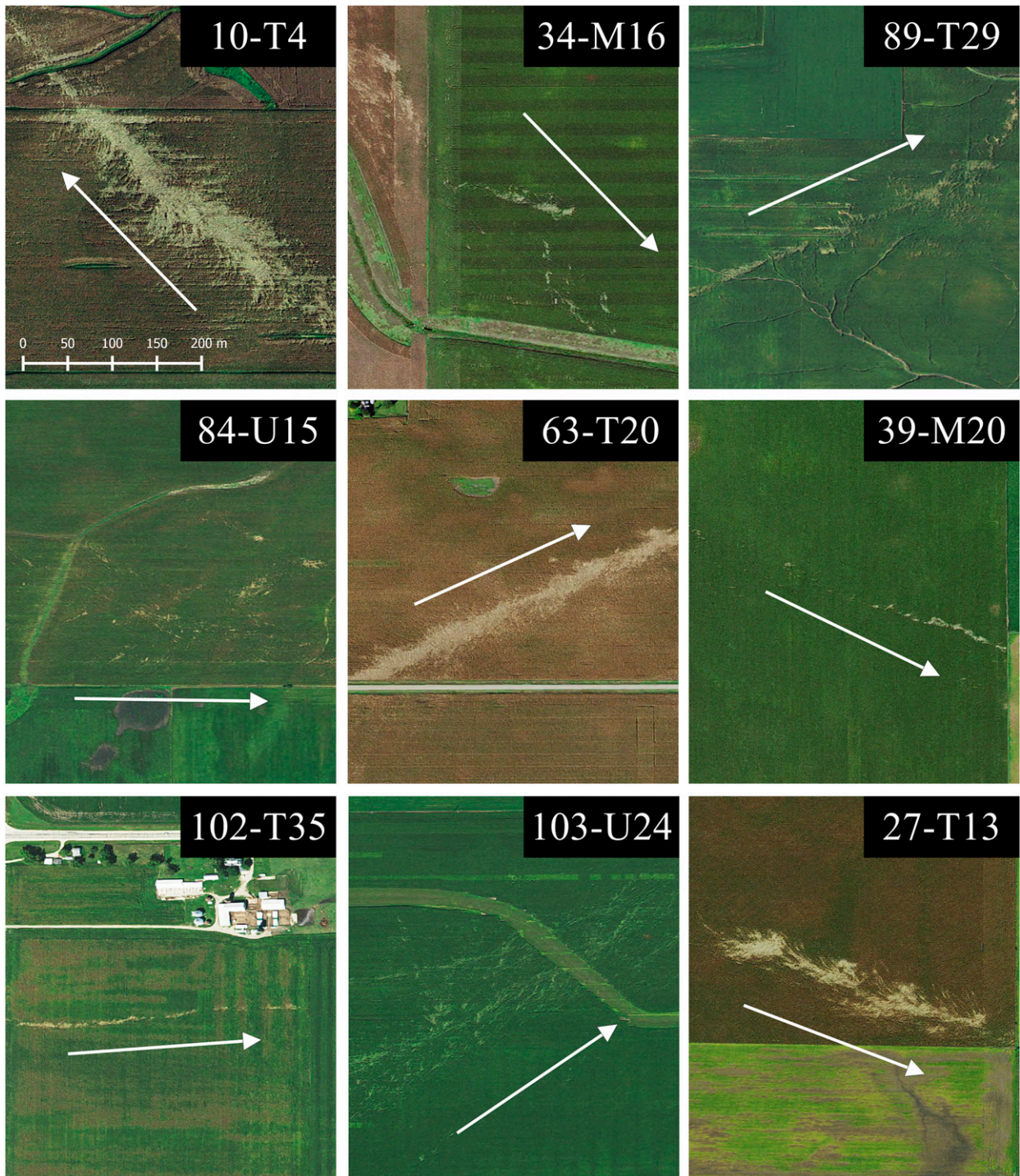
FIG. 12. NAIP imagery collage of nine tracks from 31A14, highlighting the wide variety of damage patterns observed. Track direction (arrows alongside the tracks) and identification numbers are provided with each event. All images are rendered to the same scale. Note the very broad wind patterns associated with tracks 34-M16, 84-U15, and 103-U24, in which there were only linear winds or very weak convergence.
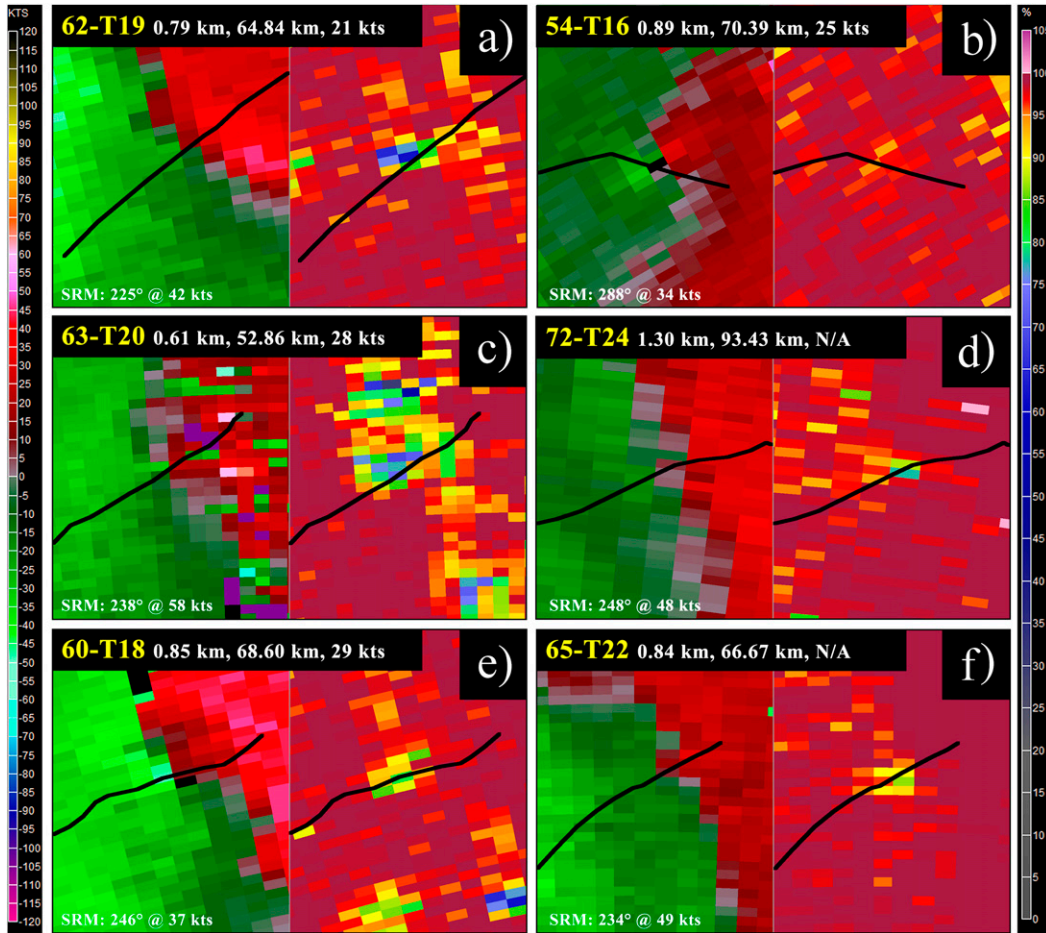
FIG. 13. A two-panel sampling of 0.5° (left) SRV and (right) ρ_{hv} for six TDSs while each respective tornado was in progress, centered on the tornado. All images are rendered to the same scale. TDS distance from KDMX and height are provided with each image along with an overlay of the tornado path with a black line. If a couplet was discernable, V_{rot} values at the time of the image are also provided (see the appendix for the maximum 0.5° V_{rot}). Tornadoes shown include (a) 62-T19, (b) 54-T16, (c) 63-T20, (d) 72-T24, (e) 60-T18, and (f) 65-T22. Note that three TDSs are visible in (e): one for 62-T19 in the bottom-right [same capture time as in (a)] and another for 56-T17 near the bottom center. The TDS for (c) is partially obscured by nonmeteorological scatterers along the leading edge of the cold pool, but possesses a depth through the radar sample volume beyond that of the cold pool ρ_{hv} minima (not shown).

aerial imagery for the 12th TDS compromised because of field harvesting. One TDS reached an estimated height of 3.47 km (measurement confidence is only moderate because of ρ_{hv} data quality issues), while the average TDS height was 1.90 km. A map of the TDS locations and tracks they were associated with is offered in Fig. 14. Of the 19 tornadoes in the Fig. 14 sample area, 57% had TDSs and 81% of the tracks within 80 km of KDMX had a TDS. Five of the 12 TDSs did not have a subjectively resolvable couplet. The remaining seven couplets were oftentimes weak and difficult to differentiate from the rest of the convergence zone with an average peak V_{rot} of only 14.8 m s^{-1}. These two facts highlight the strengths of the proposed TDS

identification technique in leveraging ρ_{hv}–min behavior and incorporating convergence zones into the TDS analysis.

b. Merging tornadoes

Scientific studies of merging tornadoes are rare, with only three probable supercell cases documented from events in 1965 (Fujita et al. 1970), 1992 (Davies et al. 1994, hereafter D94), and 2011 (French et al. 2015, hereafter F15). Aerial data for 31A14 revealed strong evidence of a merger between tornadoes 62-T19 and 64-T21 in Hamilton County, believed to be the first documented between QLCS tornadoes (see Fig. 15a for track map). The following is a best-estimate diagnosis of
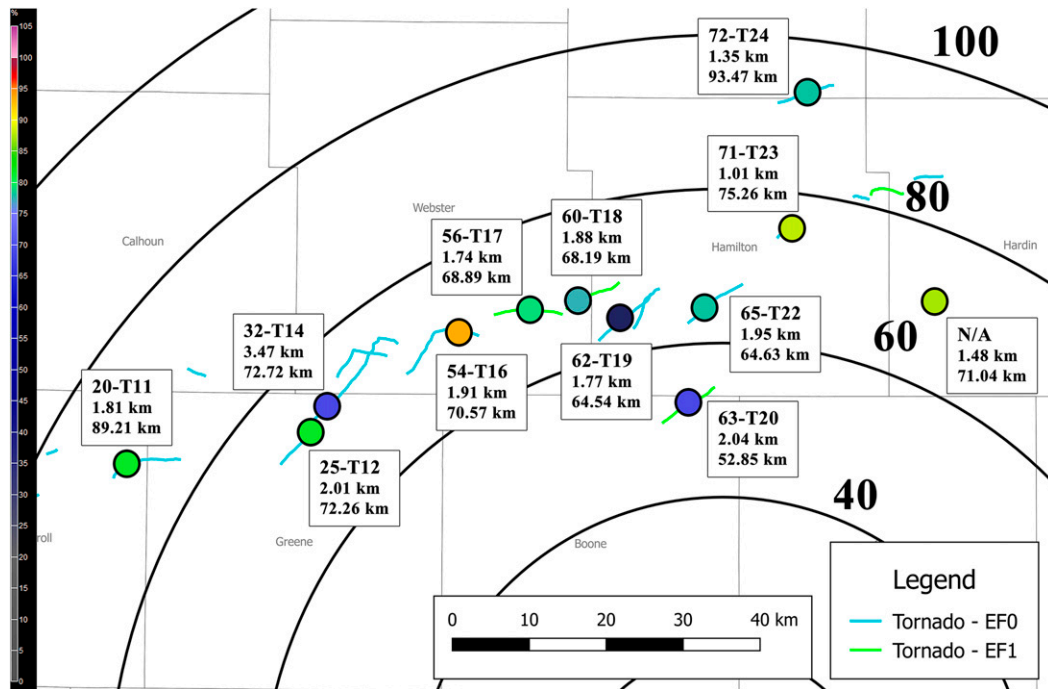
FIG. 14. Plot of the 12 TDS locations and track lines for all tornadoes within a 100-km radius of KDMX. Range rings are spaced in 20-km intervals. Round markers denote the locations of TDSs when first noted on radar while the marker color corresponds to the lowest ρ_{hv} superresolution pixel value observed during the lifespan of the TDS (at any time or elevation angle; see scale on left). Identification number, maximum TDS height, and distance from KDMX are provided with each marker.

how the merger unfolded based on radar and aerial data. Tornado 62-T19 developed immediately northeast of Stratford at 0141 UTC and tracked at an average speed of 25 m s^{-1} on a heading of 40°. Tornado 64-T21 formed 1.84 km to the southeast of 62-T19 at 0143 UTC and was comparable in both diameter (30–40 m) and crop damage intensity to 62-T19. Over the ensuing 2 min, the track of 62-T19 deviated 9° to the right of its previous heading and 64-T21 gradually accelerated along a broad cyclonic northeast-to-north arc as deduced by its elongating asymmetrically cyclonic damage striations.

By the time the two tornadoes were 700 m apart at 0145 UTC, the path characteristics of 64-T21 were difficult to determine, likely owing to its fast translational speed. Beyond this point, a broader wind field developed between the approaching vortices and eventually extended ~200 m outward along the right flank of each premerger vortex. Tornado 64-T21 passed at some distance in front of 62-T19 at ~0145:30 UTC and appears to have slowed, turned northeastward, and broadened as 62-T19 crossed its path from behind and pulled to within 250 m of the circulation on its southeast flank (Fig. 15b). However, the exact traits of the paths, especially 64-T21, at this location are not known since the underlying soybean field revealed no damage

markings (the crossing point was discernable within a cornfield). At this point, 62-T19 turned nearly due north and passed within an estimated 50–100 m ahead of 64-T21. The two vortices merged just beyond this point (Fig. 15c) at ~0146:30 UTC, and the mean circulation promptly widened to 220 m or roughly 6 times the original tornado diameters. It appears that the decaying 62-T19 wrapped around the north side of the widening vortex for a distance of ~250 m before being absorbed by 64-T21. The merger was complete after a translation distance of ~750 m, and a single cyclonic entity appears to move into the adjacent cornfield. The diffuse circulation traveled northeast for 1 km before apparently degenerating into a linear wind field at the northern apex of a developing 1.5-km-wide downburst. Nevertheless, a 100-m-wide swath of enhanced crop damage was noted for another 3.3 km downstream of the estimated end point.

The 0.5° SRV data from KDMX (beam height 750–880 m) struggled to resolve a couplet for 62-T19, with a peak V_{rot} of 10.8 m s^{-1} across the premerger couplet (Fig. 13a). While no couplet could be determined for 64-T21 prior to the merger, a 2.8-km-long ribbon of 36 m s^{-1} outbound V_r values was noted just ahead of the tornado (right side of the SRV pane in Fig. 13a). At the
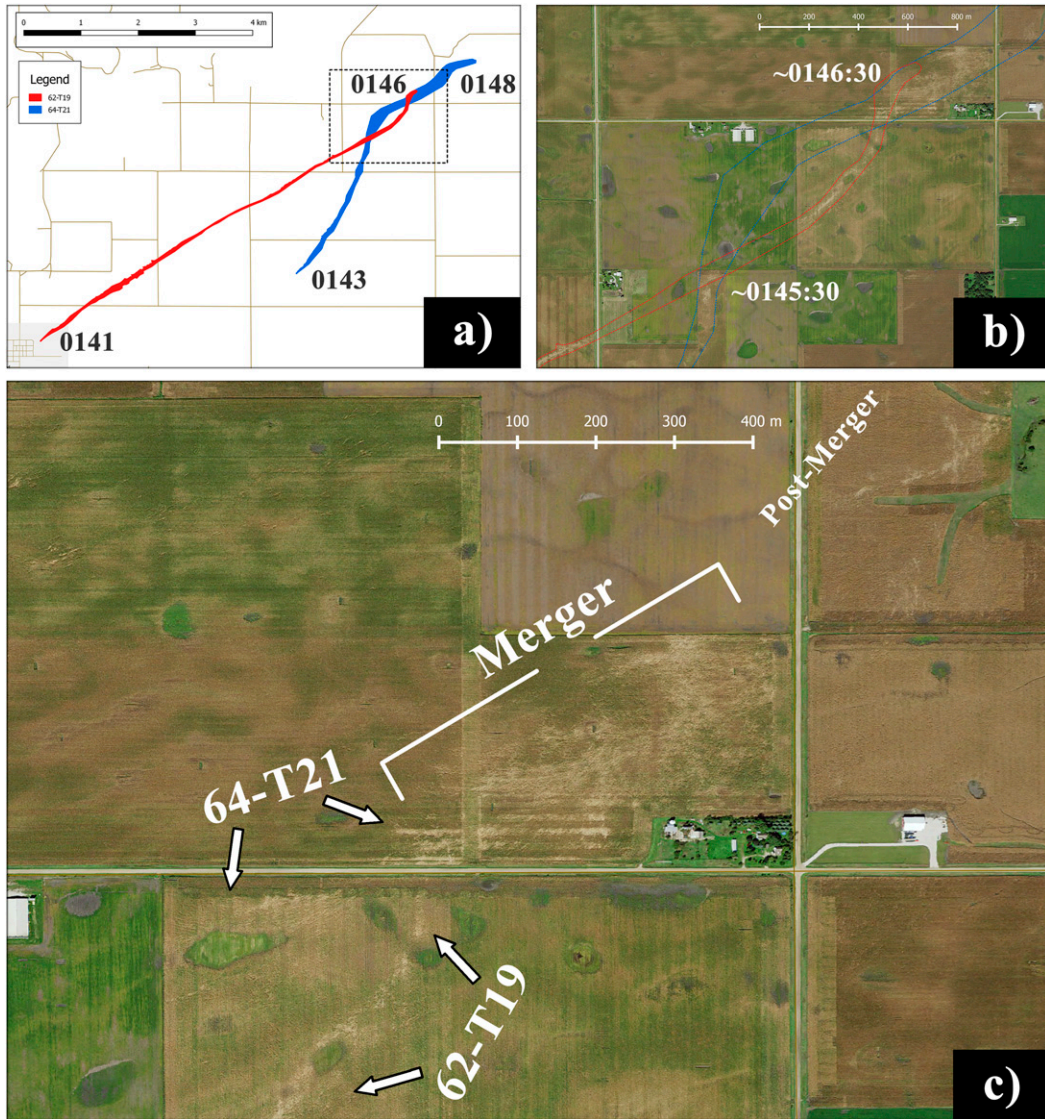
FIG. 15. (a) Polygon paths for 62-T19 (red) and 64-T21 (blue) with the start and end times for each tornado annotated. Local streets are provided as a map background. The black dotted outline denotes the region encompassed by the aerial imagery shown in (b) of both track crossing points and the merger, with the estimated times of the first crossing point and merger noted. Tracks are outlined in the same colors as (a). (c) Close-up imagery of the merger point with different stages of the merging process highlighted.

time of the merger, V_{rot} increased slightly to $11.7\,\mathrm{m\,s^{-1}}$. Beyond this point, the couplet could not be distinguished from two additional couplets developing 2–4 km farther north along the line. Despite the velocity data shortcomings, a prominent TDS was observed for 62-T19 starting with the 0143 UTC scan, extending upward to 2 km and containing values as low as 0.29 (Fig. 13a). This TDS merged with the TDS from 60-T18 at 0149 UTC, and the combined TDS persisted until 0151 UTC. A pre-merger 0.5° TDS could not be resolved during 64-T21 owing to the fact that its 3 min of existence prior to the merger was between 0.5° scans. The 1.3° ρ_{hv} product at

0144:58 UTC conceivably shows two minima embedded in a broader TDS.

The helical track behavior and structural fluctuations of the tornadoes leading up to and during the merger are remarkably similar to the TVS observations of F15 and a corotating vortex merging simulation by Meunier et al. (2005, hereafter M05). F15 used a mobile X-band phased-array radar to examine volumetric TVS trends during a tornado merger at a temporal resolution of 11 s, 13–15 times greater than 150–170-s SAILS updates from KDMX. Their radar-based couplet plots mirror the 31A14 helical ground tracks described above. While the
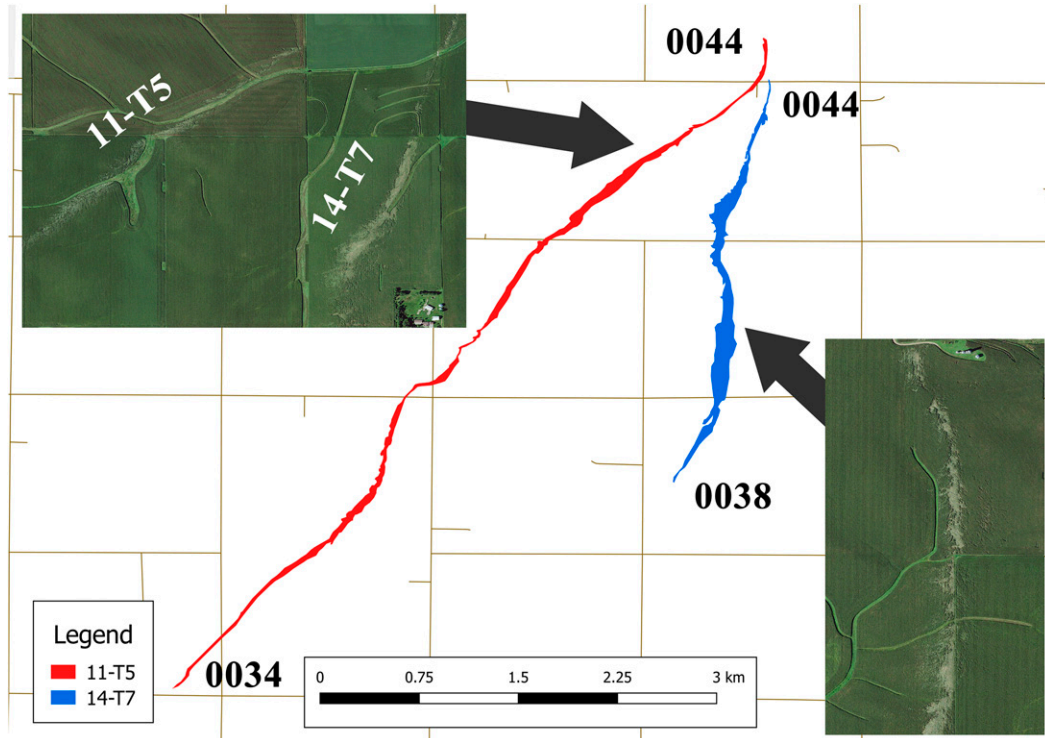
FIG. 16. Polygon paths for tornadoes 11-T5 (red) and 14-T7 (blue), using the same background as in Fig. 15a. Estimated start and end times are provided with each path along with sample inserts of the aerial imagery.

31A14 postmerger tornado did widen as noted in D94, M05, and F15, it did not appear to strengthen appreciably as D94 and F15 observed, but instead dissipated 1 km after the merger completion point.

A second case of nearly merging tornadoes occurred with 11-T5 and 14-T7 in Carroll County at 0044 UTC (Fig. 16). These two prominent tornadoes developed 2.15 km apart, with the western track (11-T5) traveling northeast and the eastern track (14-T7) translating nearly due north. The two tracks rapidly narrowed as they converged, with 14-T7 dissipating within 70 m of reaching 11-T5, which lifted shortly thereafter.

c. Tornado–cold pool interactions

Multiple instances were cataloged where the QLCS cold pool advanced faster than the tornadoes, resulting in the tornadoes occluding and falling back behind the leading edge of the cold pool. Tornado 20-T11 developed along the leading edge of the bow echo in northeast Carroll County at 0057 UTC (Fig. 17), with a small appendage noted on Z_{HH} along with a 16.3 m s^{-1} V_{rot} couplet (Fig. 18a). By 0059 UTC (Fig. 18b), a TDS was clearly visible in ρ_{hv}, although the couplet and σ_v maximum were ill-defined. The tornado appeared to occlude at this point based on the SRV couplet shifting back into the Z_{HH} shield and the ground track

heading (Fig. 17) gradually deviating from northeast to east beyond this point. The TDS was still visible at 0102 UTC (Fig. 18c) with a ρ_{hv}–min value of 0.93 and a 5.5 m s^{-1} V_{rot} couplet 3.5 km behind the leading edge of the SRV/Z_{HH}-resolved cold pool. Three minutes later (Fig. 18d), the 0.93 ρ_{hv}–min and 9.0-m s^{-1} σ_v maximum were still visible along the track 4.5 km behind the SRV convergence zone. Both signatures rapidly decayed at 0107 UTC, very near the end point of the tornado (not shown). The semi-intermittent nature of the track's last 2.5 km in the aerial data made it difficult to discern whether the circulation had transitioned into a downburst. Since the path width did not increase, it is assumed that a circulation was maintained. Tornado 16-T9 demonstrated similar attributes over a smaller spatial and temporal scale.

A more striking example of tornado–cold pool interactions transpired across a 20 km $\times$ 6 km area of southern Webster County. Between 0120 and 0130 UTC, three tornadoes (32-T14, 44-T15, and 54-T16) propagating northeastward along the leading edge of the bow echo were undercut by a second cold pool orthogonal to the convective line (Fig. 19a). While the slope of the bow echo was nearly vertical between the 0.5° and 1.8° tilts, the second boundary to the northwest contained a 20° slope between the same tilts. Extrapolating this
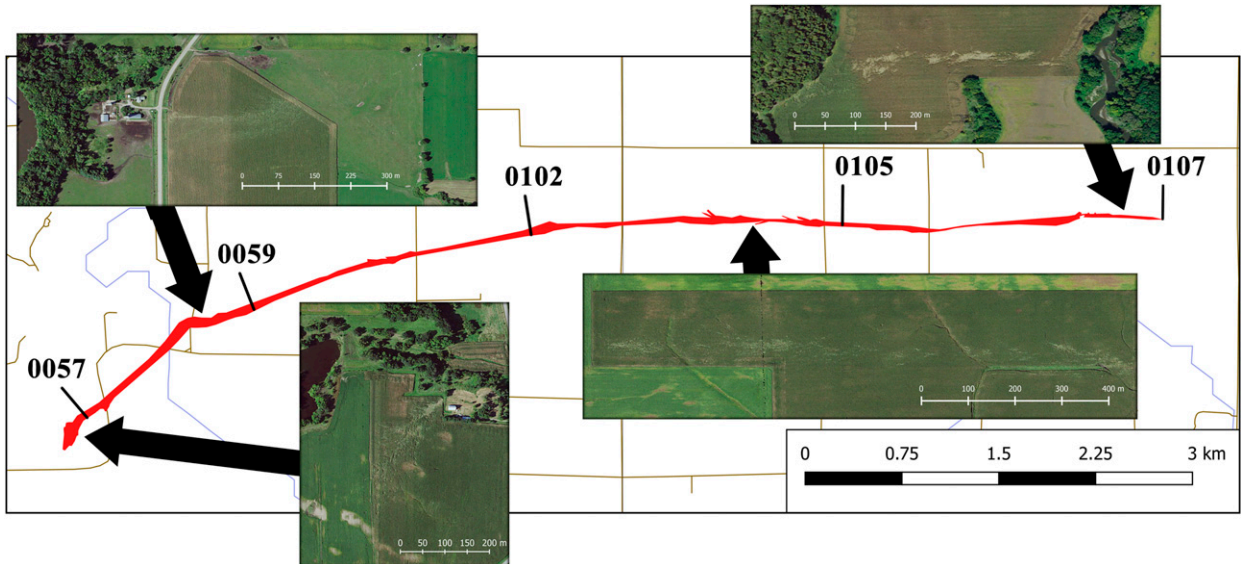
FIG. 17. Polygon path (red) for tornado 20-T11 along with time fixes derived from KDMX SRV, ρ_{hv}, and σ_v products. Roads (tan) and rivers (blue) are provided for background reference. Sample inserts of aerial imagery are provided at several points along the track.

slope to the surface would place the boundary 2.95 km ahead of the radar-resolved placement. This spatial shift would place the boundary very near the three tornadoes at the times of occlusion. In each case, the surface circulations widened, made a hard turn to the east-southeast, and sheared apart 2.5–5.8 km after making the turn. Figures 19b–d showcase the evolution of 54-T16 in the aerial dataset. Level II radar data are unavailable for a substantial portion of this time frame, but two scans at 0133 UTC (Fig. 13b) and
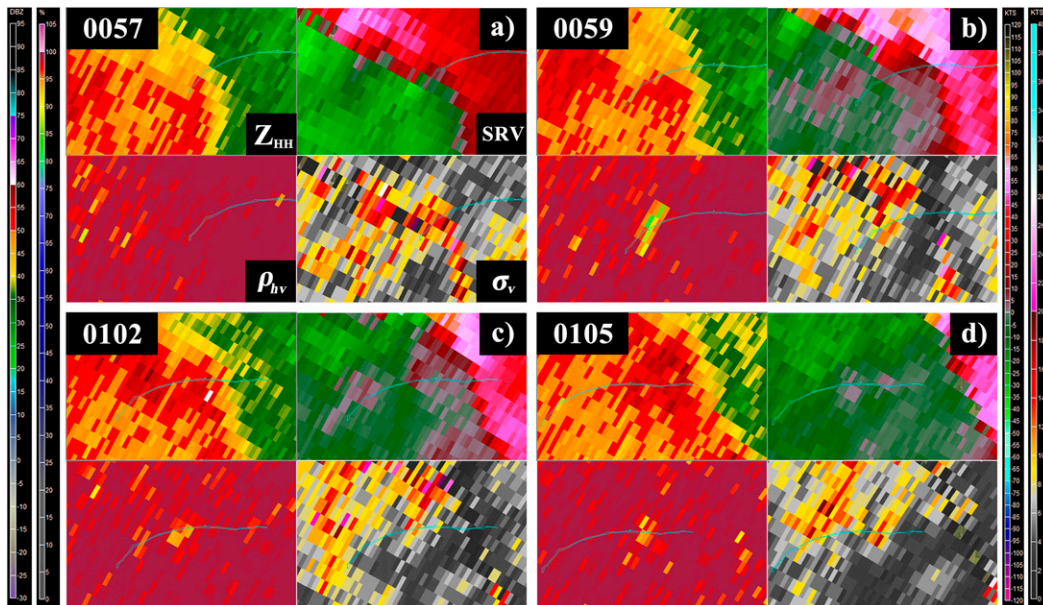
FIG. 18. Feature-following, four-panel (top left, Z_{HH}; top right, SRV; bottom left, ρ_{hv}; bottom right, σ_v) KDMX radar images of 20-T11 at (a) 0057 UTC (SAILS), (b) 0059 UTC, (c) 0102 UTC (SAILS), and (d) 0105 UTC. Range to KDMX varies from 83.48 to 89.64 km and height likewise varies between 1.10 and 1.22 km. The tornado path polygon (blue) is overlaid for reference. SRM is set to 209° at 29 kt (14.9 m s^{-1}) for (a) with all other SRV pane SRMs set to 259° at 30 kt (15.4 m s^{-1}).
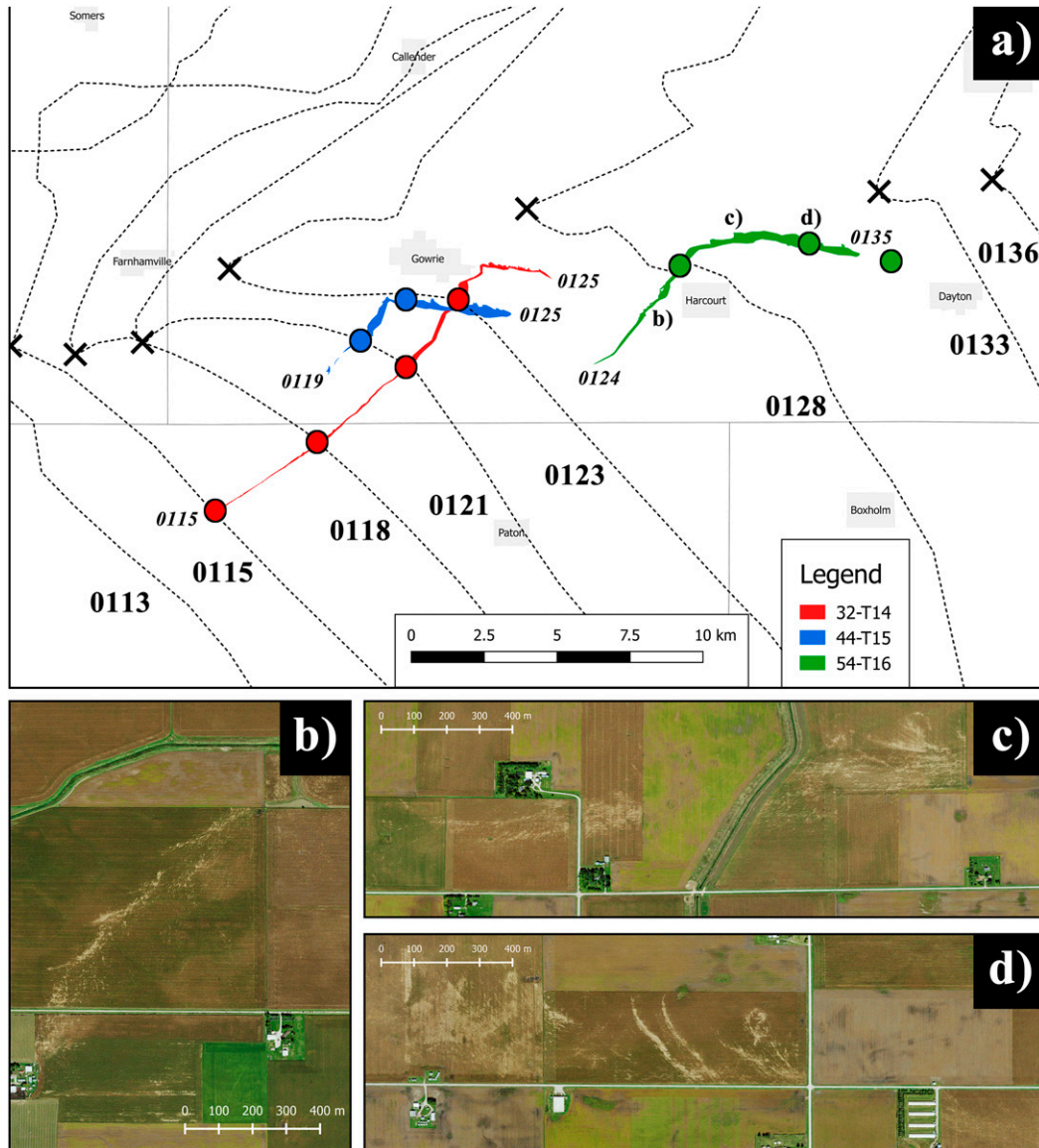
FIG. 19. (a) Polygon paths of 32-T14 (red), 44-T15 (blue), and 54-T16 (green) along with the leading edge of both cold pools (dashed lines, with exes denoting the boundary intersection) as resolved by KDMX 0.5° V_r at a height of 820–1100 m. Tornado positions derived via 0.5°SRV/ρ_{hv} and plotted as circles at the same temporal interval as the boundaries, along with their estimated begin and end times (in italics). The extra marker following 54-T16 corresponds to the couplet/TDS location just beyond the surface circulation dissipation point. The letters next to the path of 54-T16 correspond to aerial photos showcasing the evolution of the track (b) before, (c) during, and (d) after the interaction with the secondary cold pool.

0136 UTC show a pronounced 13.0 m s^{-1} V_{rot} couplet and faint TDS for 54-T16 displaced over 5 km behind the leading edge of the cold pool.

5. Discussion

a. Genesis processes

QLCS tornado research over the past two decades has focused primarily on the mesovortex, a low-level meso-γ circulation that typically develops along and north of a convective bow segment and has been shown to be coincident with tornadoes and damaging wind swaths (Przybylinski 1995; WT03). Mesovortex genesis theories vary, but many focus on the tilting of baroclinically generated horizontal vorticity into a vertical orientation via different mechanisms (Trapp and Weisman 2003; WT03; Atkins and St. Laurent 2009b). Several mesovortices were noted throughout the middle
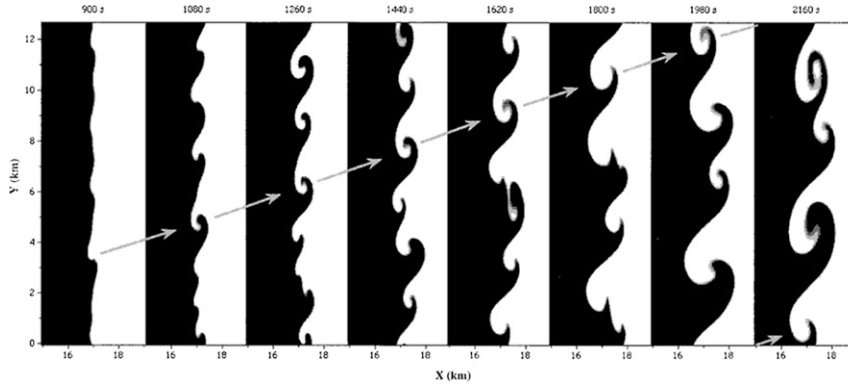
FIG. 20. Horizontal cross section through the leading edge of a simulated outflow boundary at $z = 0.55$ km featuring the development of misocyclone circulations. The abrupt shading change denotes the approximate -3-K perturbation potential temperature value. Note that individual misocyclone evolutions may be tracked in time by visually following their thermal signature north on each subsequent 180-s time interval [original from Lee and Wilhelmson (1997, Fig. 6)].

to latter stages of 31A14 once multiple bowing segments materialized, and most were associated with narrow corridors of wind damage and localized surface circulations. Nevertheless, numerous tornadoes on 31A14 were not observed on radar to be associated with mesovortices on the scales described in the previous literature. In fact, even at 50–90 km from KDMX, some of the strongest tornadoes during the event were only discernable in SRV as one superresolution inbound and outbound range gate, if at all (Figs. 13a–f). In addition, couplets were often only visible coincident with or after tornadogenesis. Based on the scale and behavior of these couplets, it would appear that the mechanisms shown in previous studies to generate mesovortices were not present in the genesis of many 31A14 tornadoes.

Early studies of QLCS tornadoes proposed that horizontal shearing instability may be responsible for QLCS
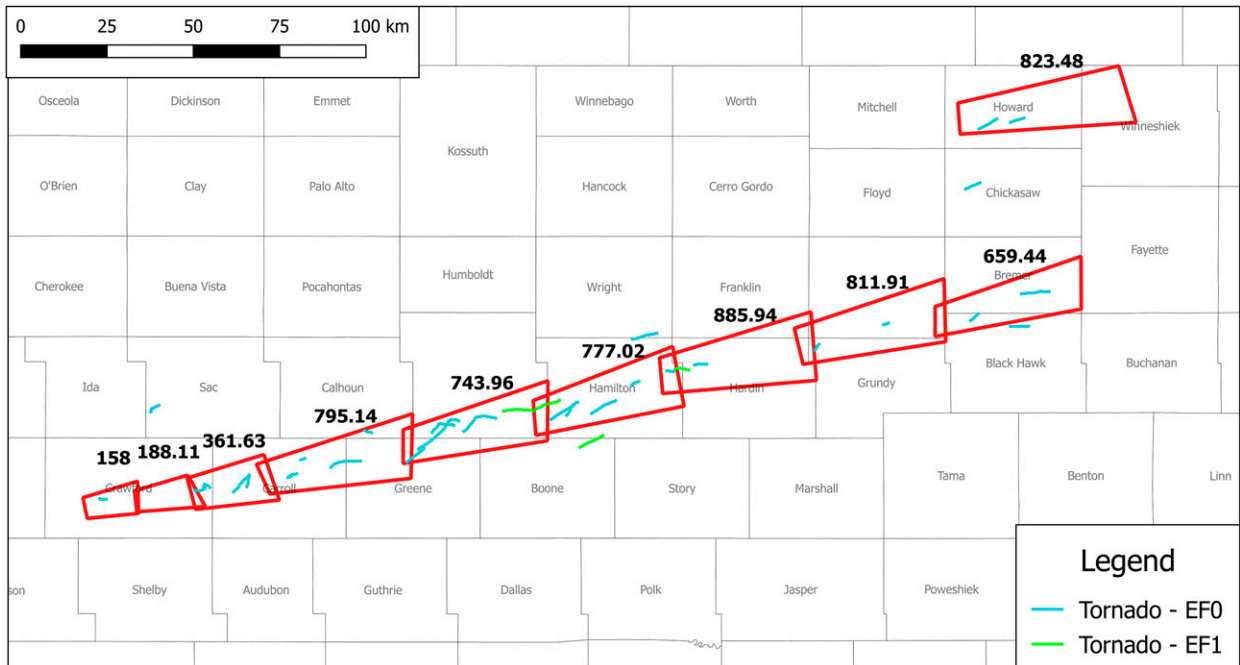
FIG. 21. Map of all 31A14 tornadoes with hypothetical tornado warnings (red) overlaid to cover as many tornadoes as possible, based on storm structure recognition and ambient environment. Warning duration set to 45 min for the western-most warning and 30 min for all subsequent warnings. Warning area (km^2) noted above each polygon and determined by the storm motion and structure at issuance time. The combined tornado warning area amounts to 6204.63 km^2, while the collective tornado path area amounts to 15.06 km^2, only 0.242% of the combined warning polygon size.

TABLE A1. Chronologic listing and select attributes of 31A14 damage paths. Width refers to the maximum damage track width. TDS height refers to the highest height of the ρ_{hv} minima meeting the criteria outlined in section 2a; it does not include one TDS for which no track could be located. For V_{rot}, maximum V_{rot} values only calculated for subjectively resolved, gate-to-gate SRV couplets. For the test score, fields with the prefix T- denote tornadoes that satisfied either the TDS/structural damage (T-2) or combined pathlength/crop damage (T-3) tests. Numeric-only entries represent the score of tracks that did not pass the two aforementioned tests. The testing scheme is outlined in Fig. 4.

ID	County	Time (UTC)	Length (km)	Width (m)	EF scale	TDS height (km, ARL)	V_{rot} (m s^{-1})	Test score
1-U1	Crawford	2322–2322	0.37	87				5
2-U2	Crawford	2326–2326	0.45	78				4
3-T1	Crawford	2333–2338	2.11	302	0		16.5	10
4-U3	Crawford	2342–2342	0.14	32				4
5-T2	Sac	2344–2350	3.98	55	0			T-2
6-M1	Crawford	0019–0020	0.55	18				1
7-M2	Crawford	0023–0024	0.58	23			21.8	3
8-M3	Sac	0025–0026	1.66	37				1
9-T3	Crawford	0026–0029	3.19	64	0		20.7	7
10-T4	Crawford	0030–0032	1.14	146	0			7
11-T5	Carroll	0034–0044	8.27	82	0			T-2
12-T6	Crawford	0035–0038	1.51	64	0		7.5	7
13-M4	Crawford	0036–0036	0.68	18				2
14-T7	Carroll	0038–0044	4.25	128	0			T-3
15-T8	Carroll	0045–0047	1.13	73	0		10.5	T-2
16-T9	Carroll	0047–0052	2.54	183	0		11.0	T-3
17-M5	Carroll	0051–0051	0.39	18				1
18-M6	Carroll	0054–0054	0.53	18				1
19-T10	Carroll	0054–0055	1.24	55	0			T-2
20-T11	Carroll–Greene	0057–0107	9.45	91	0	1.81	16.3	T-2
21-M7	Greene	0109–0109	0.43	9				1
22-M8	Calhoun	0110–0110	0.92	18				1
23-M9	Calhoun	0111–0111	0.35	9				1
24-U4	Greene	0111–0113	3.11	128			17.8	5
25-T12	Greene	0111–0116	7.26	41	0	2.01		T-2
26-M10	Greene	0112–0112	0.32	41				1
27-T13	Calhoun	0113–0114	2.27	91	0			T-2
28-M11	Calhoun	0113–0115	2.67	78				2
29-M12	Calhoun	0114–0114	0.63	46				1
30-M13	Calhoun	0115–0115	0.93	32				1
31-M14	Greene	0115–0115	0.50	32				2
32-T14	Greene–Webster	0115–0125	17.61	329	0	3.47	23.5	T-2
33-M15	Greene	0116–0116	0.39	23				1
34-M16	Calhoun	0116–0117	2.85	82				3
35-M17	Calhoun	0117–0117	0.56	37				1
36-M18	Calhoun	0118–0118	1.09	37				2
37-M19	Webster	0118–0118	0.47	27				2
38-U5	Webster	0118–0118	0.77	69				5
39-M20	Calhoun–Webster	0118–0119	1.58	37				3
40-M21	Webster	0119–0119	0.13	9				1
41-M22	Calhoun–Webster	0119–0120	1.56	27				3
42-M23	Webster	0119–0120	0.77	37				1
43-U6	Webster	0119–0122	2.74	23				4
44-T15	Webster	0119–0125	8.34	366	0		29.7	T-3
45-U7	Webster	0120–0121	2.20	91			20.5	5
46-M24	Calhoun	0121–0121	0.48	18				1
47-M25	Greene	0121–0121	0.42	18				1
48-M26	Guthrie	0121–0121	0.31	23				1
49-U8	Webster	0121–0122	1.26	41				6
50-M27	Webster	0122–0122	0.64	14				1
51-M28	Webster	0123–0124	2.43	73				3
52-M29	Webster	0124–0124	0.93	46				1
53-M30	Webster	0124–0124	0.47	9				1

TABLE A1. (*Continued*)

ID	County	Time (UTC)	Length (km)	Width (m)	EF scale	TDS height (km, ARL)	V_{rot} (m s^{-1})	Test score
54-T16	Webster	0124–0135	12.28	521	0	1.91	13.0	T-2
55-U9	Webster	0127–0129	3.15	18				4
56-T17	Webster	0135–0141	8.75	91	1	1.74	9.5	T-2
57-M31	Webster	0138–0138	0.29	41				1
58-M32	Boone	0138–0139	1.27	37				2
59-M33	Dallas	0139–0139	0.37	14				1
60-T18	Webster–Hamilton	0140–0145	7.61	187	1	1.88	16.5	T-2
61-M34	Dallas	0141–0141	0.19	9				1
62-T19	Hamilton	0141–0146	8.96	101	0	1.77	10.8	T-2
63-T20	Boone–Hamilton	0143–0148	8.03	137	1	2.04	14.5	T-2
64-T21	Hamilton	0143–0148	6.21	219	0		11.7	T-2
65-T22	Hamilton	0146–0152	8.55	59	0	1.95		T-2
66-M35	Hamilton	0149–0149	0.47	27			8.2	3
67-U10	Hamilton	0150–0151	1.17	201			6.0	5
68-U11	Hamilton	0152–0154	2.66	320			13.2	4
69-M36	Cerro Gordo	0156–0157	1.11	14				1
70-M37	Hamilton	0157–0157	1.05	46				2
71-T23	Hamilton	0158–0200	2.43	69	0	1.01		T-2
72-T24	Hamilton–Wright	0159–0204	7.40	110	0	1.35		T-2
73-M38	Wright	0205–0205	0.37	37				2
74-M39	Wright	0205–0205	0.58	27				2
75-M40	Wright	0206–0206	0.93	69				1
76-T25	Hamilton	0206–0207	1.88	55	0			T-2
77-U12	Franklin	0207–0210	3.94	101				5
78-T26	Hamilton–Hardin	0208–0210	4.60	155	1			T-2
79-U13	Hardin	0209–0212	3.56	37				5
80-T27	Hardin	0211–0213	3.56	69	0			8
81-M41	Hardin	0214–0215	1.79	73				3
82-M42	Hardin	0218–0218	0.98	73				1
83-U14	Hardin	0218–0218	1.17	101				4
84-U15	Hardin	0218–0219	2.24	251				4
85-M43	Hardin	0219–0219	1.17	55				1
86-U16	Adair	0223–0224	1.43	46			10.8	4
87-T28	Grundy	0235–0237	2.62	69	0			8
88-U17	Butler	0239–0242	3.22	55				6
89-T29	Butler	0249–0250	1.69	37	0			7
90-U18	Butler	0251–0253	2.80	59				5
91-M44	Butler	0253–0253	0.31	27				2
92-T30	Chickasaw	0300–0304	4.81	55	0			T-2
93-U19	Butler–Bremer	0301–0304	3.41	64				4
94-U20	Bremer	0302–0303	1.24	78				4
95-T31	Black Hawk	0304–0307	3.35	119	0			T-2
96-U21	Howard	0305–0306	1.00	23				4
97-T32	Howard	0308–0312	6.26	73	0			T-2
98-U22	Chickasaw	0310–0313	3.80	178				5
99-T33	Howard	0312–0315	4.20	55	0			9
100-T34	Black Hawk	0312–0317	5.25	73	0			T-3
101-U23	Chickasaw	0316–0319	4.07	183				5
102-T35	Bremer	0317–0324	8.01	91	0			T-3
103-U24	Howard	0317–0318	1.85	183				4
104-M45	Howard	0320–0321	1.37	46				2
105-M46	Bremer	0322–0322	0.31	37				3
106-M47	Fayette	0337–0337	0.35	18				1
107-M48	Fayette	0342–0342	0.35	27				2
108-M49	Fayette	0342–0342	0.21	9				1
109-M50	Fayette	0343–0343	0.66	27				1
110-M51	Fayette	0350–0350	0.34	27				1
111-U25	Fayette	0350–0352	2.54	78				4

tornadogenesis (Przybylinski 1995; Funk et al. 1999; Trapp et al. 1999). This process arises when horizontal wind shear and vertical vorticity are generated along surface boundaries as a result of large wind shifts and airmass density differences. This vorticity can undergo stretching via a convective updraft and become a tornado, akin to a landspout or waterspout (Wakimoto and Wilson 1989). FW83 suspected this mechanism to be the probable cause of tornadogenesis in their study. Figure 20, which is taken from Lee and Wilhelmson (1997), provides a horizontal cross section of shear-induced vortices generated along the leading edge of a simulated outflow boundary. The horizontal spacing of these vortices, along with their size and evolution, bear striking similarities to the aerial and radar signatures of multiple 31A14 tornadoes, most prominently those shown in Fig. 19a. It is beyond the scope of this paper to firmly classify the tornadogenesis processes of 31A14, but the evidence presented herein points toward shear instability being the primary driver of these surface circulations. Multiple facets of the aerial and radar data strongly suggest that the surface vortices we classified as tornadoes extended to the cloud base and met the formal definition of a tornado (AMS 2013). This includes the collocation of couplets and TDSs with these tracks at close radar sampling ranges, the intensity and longevity of the damage tracks, and the location of the vortices along favored tornadogenesis regions of the convective line (Schaumann and Przybylinski 2012; Schenkman and Xue 2016).

b. NWS warning and documentation challenges

The 35 tornadoes from 31A14 present two unique challenges to NWS WFOs. First, given the prolific production of tornadoes with relatively minimal damage, how best does the NWS warn for the expected level of impacts? An attempt to issue tornado warnings for all of these tornadoes would not be practical or even preferred if it leads to overwarning (see example in Fig. 21), the so-called crying wolf scenario (Trainor et al. 2015). The current NWS Impact-Based Warning demonstration (NWS 2015) provides a mechanism for forecasters to express a level of threat through the use of warning tags. For situations when forecaster confidence is not high enough to issue a tornado warning, a severe thunderstorm warning with a ''tornado possible'' tag may be issued instead. The tornado possible tag has also been used in events that pose a higher risk of poorly visible, weak (EF0/1), and transient tornadoes. The 31A14 event fits the above scenario, and this warning philosophy may better convey the level of impact inherent with many QLCSs. However, the use of this tag should not replace tornado warnings in those instances where radar and/or visual spotting strongly suggest the presence of a

damaging tornado regardless of storm mode. The conundrum lies in the present verification of these weak tornadoes. Without a tornado warning, these count as a missed event. The NWS currently issues warnings for all weather phenomena above a certain severity threshold—except tornadoes. All tornadoes, regardless of severity, longevity, or impacts, count equally for verification purposes (NWS 2016). Cases such as those from 31A14, which appear to resolve the very lower-bound spectrum of tornado circulations, lend credence to the argument that such criteria may need revisiting and to reserve tornado warnings for tornadic events that have a higher likelihood of posing a significant risk to life and property.

Documenting these events in *Storm Data* poses the second challenge to WFOs. The techniques used by the authors were unorthodox from an operational perspective since most WFOs do not have timely access to aerial imagery, if at all. In addition, the time and resources needed to study the imagery for circulations would normally be prohibitive for WFOs. Differences in land cover also play a direct role in an office's ability to document damage tracks. One of the consequences of this study was a 1650% increase in the number of documented tornadoes for 31A14 (from 2 to 35). This is not surprising given the limitations of ground-based surveys and rural reports, which frequently render an incomplete account of an event's true scope compared to aerial imagery. The usage of aerial imagery in tornado documentation would introduce a bias within *Storm Data* compared with other WFOs or events constrained to more traditional surveying methods. Putting the event in context, the 35 tornadoes from 31A14 would rank as the greatest single-day tornado outbreak in Iowa history versus the previous record of 28 tornadoes from 11 April 2001. Greg Carbin, former warning coordination meteorologist (WCM) at the SPC, suggested in a personal communication that many tornadoes analogous to those from 31A14 would have been historically entered as thunderstorm wind damage without the added benefit of the aerial imagery.

6. Conclusions and a look ahead

Aerial imagery captured following 31A14 provides a truly unique opportunity to assess the spatial distribution and track characteristics of surface circulations generated throughout the lifespan of a QLCS. The probabilistic taxonomic scheme developed for 31A14 binned 35 of the 111 paths as tornadoes and can be applied to other aerial QLCS studies in the absence of additional datasets. This is just one possible method for cataloging the wide spectrum of tracks that may be observed following a QLCS, but appears to provide a good

balance between assorted track characteristics and radar data. A new, behavioral-based TDS identification strategy better suited for convective modes such as QLCSs that may not fit the currently established threshold-based criteria is also proposed. Twelve TDSs were detected on 31A14 using this process, a number of which possessed either weak or unresolvable SRV rotational couplets.

This case illustrates how aerial datasets can dramatically alter our understanding of how a given event transpired, which has far-reaching implications for both the operational and research communities. The quantity, quality, and accessibility of high-resolution aerial and satellite datasets have improved significantly over the past two decades; one only needs to consider programs such as Google Earth (https://www.google.com/earth/), various georeferencing websites, the NAIP, and even the NWS postdisaster satellite acquisition program to comprehend its ubiquity. Another aerial surveying technology growing in popularity is unmanned aerial vehicles (UAVs), which have the same potential to revolutionize storm surveying as other aerial data sources. NOAA is currently exploring the use of UAVs for NWS storm surveys (SBIR 2015).

As aerial and satellite datasets mature, it is inevitable that similar events will be uncovered with increasing frequency and the question of how the NWS should approach these situations will need to be addressed. WT03 stated at the conclusion of their study that ''unfortunately, neither this study nor even the more recent observational studies. . .possesses the information needed for a detailed comparison with our idealized simulations.'' This study provides the first near-complete aerial assessment of a tornadic QLCS in conjunction with high-resolution, polarimetric WSR-88D data. It is hoped that this aerial study, and others that will undoubtedly follow in the coming years, provides the needed ground truth to advance the scientific understanding of QLCS tornadogenesis.

APPENDIX

Chronologic Listing and Select Attributes of 31A14 Damage Paths

Table A1 lists the attributes associated with the damage paths from 31A14.

REFERENCES

AMS, 2013: Tornado. Glossary of Meteorology. [Available online at http://glossary.ametsoc.org/wiki/Tornado.]

Atkins, N. T., and M. St. Laurent, 2009a: Bow echo mesovortices. Part I: Processes that influence their damaging potential. *Mon. Wea. Rev.*, **137**, 1497–1513, doi:10.1175/2008MWR2649.1.

——, and ——, 2009b: Bow echo mesovortices. Part II: Their genesis. *Mon. Wea. Rev.*, **137**, 1514–1532, doi:10.1175/2008MWR2650.1.

——, C. S. Bouchard, R. W. Przybylinski, R. J. Trapp, and G. Schmocker, 2005: Damaging surface wind mechanisms within the 10 June 2003 Saint Louis bow echo during BAMEX. *Mon. Wea. Rev.*, **133**, 2275–2296, doi:10.1175/MWR2973.1.

Bodine, D., M. R. Kumjian, R. D. Palmer, P. L. Heinselman, and A. V. Ryzhkov, 2013: Tornado damage estimation using polarimetric radar. *Wea. Forecasting*, **28**, 139–158, doi:10.1175/WAF-D-11-00158.1.

Bothwell, P. D., J. A. Hart, and R. L. Thompson, 2002: An integrated three-dimensional objective analysis scheme in use at the Storm Prediction Center. Preprints, *21st Conf. on Severe Local Storms/19th Conf. on Weather Analysis and Forecasting/ 15th Conf. on Numerical Weather Prediction*, San Antonio, TX, Amer. Meteor. Soc., J117–J120. [Available online at https://ams.confex.com/ams/pdfpapers/47482.pdf.]

Brotzge, J. A., S. E. Nelson, R. L. Thompson, and B. T. Smith, 2013: Tornado probability of detection and lead time as a function of convective mode and environmental parameters. *Wea. Forecasting*, **28**, 1261–1276, doi:10.1175/WAF-D-12-00119.1.

Brown, R. A., and V. T. Wood, 2012: The tornadic vortex signature: An update. *Wea. Forecasting*, **27**, 525–530, doi:10.1175/WAF-D-11-00111.1.

——, L. R. Lemon, and D. W. Burgess, 1978: Tornado detection by pulsed Doppler radar. *Mon. Wea. Rev.*, **106**, 29–38, doi:10.1175/1520-0493(1978)106<0029:TDBPDR>2.0.CO;2.

Burgess, D., and Coauthors, 2014: 20 May 2013 Moore, Oklahoma, tornado: Damage survey and analysis. *Wea. Forecasting*, **29**, 1229–1237, doi:10.1175/WAF-D-14-00039.1.

Camp, J. P., K. Stellman, and J. Settelmaier, 2010: Utilizing mobile devices for enhanced storm damage surveys. *26th Conf. on Integrated Information Processing Systems (IIPS) for Meteorology, Oceanography, and Hydrology*, Atlanta, GA, Amer. Meteor. Soc., 5B.4. [Available online at ams.confex.com/ams/90annual/webprogram/Paper161540.html.]

——, L. P. Rothfusz, A. Anderson, D. Speheger, K. L. Ortega, and B. R. Smith, 2014: Assessing the Moore, Oklahoma (2013) tornado using the National Weather Service Damage Assessment Toolkit. *Special Symp. on Severe Local Storms: The Current State of the Science and Understanding Impacts*, Atlanta, GA, Amer. Meteor. Soc., 830. [Available online at https://ams.confex.com/ams/94Annual/webprogram/Paper233734.html.]

Church, C. R., J. T. Snow, G. L. Baker, and E. M. Agee, 1979: Characteristics of tornado-like vortices as a function of swirl ratio: A laboratory investigation. *J. Atmos. Sci.*, **36**, 1755–1766, doi:10.1175/1520-0469(1979)036<1755:COTLVA>2.0.CO;2.

Davies, J. M., C. A. Doswell III, D. W. Burgess, and J. F. Weaver, 1994: Some noteworthy aspects of the Hesston, Kansas, tornado family of 13 March 1990. *Bull. Amer. Meteor. Soc.*, **75**, 1007–1017, doi:10.1175/1520-0477(1994)075<1007:SNAOTH>2.0.CO;2.

Davies-Jones, R. P., 1986: Tornado dynamics. *Thunderstorms: A Social and Technological Documentary*, E. Kessler, Ed., Vol. II, University of Oklahoma Press, 197–236.

Edwards, R., J. G. LaDue, J. T. Ferree, K. Scharfenberg, C. Maier, and W. L. Coulbourne, 2013: Tornado intensity estimation: Past, present, and future. *Bull. Amer. Meteor. Soc.*, **94**, 641–653, doi:10.1175/BAMS-D-11-00006.1.

Entremont, C., and J. D. Lamb, 2015: The relationship between tornadic debris signature height and tornado intensity. *Third Symp. on Building a Weather-Ready Nation: Enhancing Our Nation's Readiness, Responsiveness, and Resilience to High Impact Weather Events*, Phoenix, AZ, Amer. Meteor. Soc., 452. [Available online at https://ams.confex.com/ams/95Annual/webprogram/Paper268874.html.]

Forbes, G. S., and R. M. Wakimoto, 1983: A concentrated outbreak of tornadoes, downbursts and microbursts, and implications regarding vortex classification. *Mon. Wea. Rev.*, **111**, 220–235, doi:10.1175/1520-0493(1983)111<0220:ACOOTD>2.0.CO;2.

French, M. M., P. S. Skinner, L. J. Wicker, and H. B. Bluestein, 2015: Documenting a rare tornado merger observed in the 24 May 2011 El Reno–Piedmont, Oklahoma, supercell. *Mon. Wea. Rev.*, **143**, 3025–3043, doi:10.1175/MWR-D-14-00349.1.

Fujita, T. T., 1974: Jumbo tornado outbreak of 3 April 1974. *Weatherwise*, **27** (3), 116-126, doi:10.1080/00431672.1974.9931693.

——, 1978: Manual of downburst identification for Project NIMROD. SMRP Research Paper 156, University of Chicago, 104 pp.

——, 1981: Tornadoes and downbursts in the context of generalized planetary scales. *J. Atmos. Sci.*, **38**, 1511–1534, doi:10.1175/1520-0469(1981)038<1511:TADITC>2.0.CO;2.

——, and A. D. Pearson, 1973: Results of FPP classification of 1971 and 1972 tornadoes. Preprints, *Eighth Conf. on Severe Local Storms*, Denver, CO, Amer. Meteor. Soc., 142–145.

——, D. L. Bradbury, and C. F. Van Thullenar, 1970: Palm Sunday tornadoes of April 1, 1965. *Mon. Wea. Rev.*, **98**, 29–69, doi:10.1175/1520-0493(1970)098<0029:PSTOA>2.3.CO;2.

Funk, T. W., K. E. Darmofal, J. D. Kirkpatrick, V. L. Dewald, R. W. Przybylinski, G. K. Schmocker, and Y.-J. Lin, 1999: Storm reflectivity and mesocyclone evolution associated with the 15 April 1994 squall line over Kentucky and southern Indiana. *Wea. Forecasting*, **14**, 976–993, doi:10.1175/1520-0434(1999)014<0976:SRAMEA>2.0.CO;2.

Jedlovec, G. J., U. Nair, and S. L. Haines, 2006: Detection of storm damage tracks with EOS data. *Wea. Forecasting*, **21**, 249–267, doi:10.1175/WAF923.1.

Karstens, C. D., T. M. Samaras, B. D. Lee, W. A. Gallus Jr., and C. A. Finley, 2010: Near-ground pressure and wind measurements in tornadoes. *Mon. Wea. Rev.*, **138**, 2570–2588, doi:10.1175/2010MWR3201.1.

——, W. A. Gallus Jr., B. D. Lee, and C. A. Finley, 2013: Analysis of tornado-induced tree fall using aerial photography from the Joplin, Missouri, and Tuscaloosa–Birmingham, Alabama, tornadoes of 2011. *J. Appl. Meteor. Climatol.*, **52**, 1049–1068, doi:10.1175/JAMC-D-12-0206.1.

Lee, B. D., and R. B. Wilhelmson, 1997: The numerical simulation of non-supercell tornadogenesis. Part I: Initiation and evolution of pretornadic misocyclone circulations along a dry outflow boundary. *J. Atmos. Sci.*, **54**, 32–60, doi:10.1175/1520-0469(1997)054<0032:TNSONS>2.0.CO;2.

Lemon, L. R., 1999: Operational uses of velocity spectrum width data. Preprints, *29th Int. Conf. on Radar Meteorology*, Montreal, QC, Canada, Amer. Meteor. Soc., 776–779.

Lewellen, D. C., W. S. Lewellen, and J. Xia, 2000: The influence of a local swirl ratio on tornado intensification near the surface. *J. Atmos. Sci.*, **57**, 527–544, doi:10.1175/1520-0469(2000)057<0527:TIOALS>2.0.CO;2.

Lewellen, W. S., 1993: Tornado vortex theory. *The Tornado: Its Structure, Dynamics, Prediction and Hazards*, Geophys. Monogr., Vol. 79, Amer. Geophys. Union, 19–39.

McDonald, J. R., 2001: T. Theodore Fujita: His contribution to tornado knowledge through damage documentation and the Fujita scale. *Bull. Amer. Meteor. Soc.*, **82**, 63–72, doi:10.1175/1520-0477(2001)000<0063:TTFHCT>2.3.CO;2.

Meunier, P., S. Le Dizès, and T. Leweke, 2005: Physics of vortex merging. *C. R. Phys.*, **6**, 431–450, doi:10.1016/j.crhy.2005.06.003.

Moller, A. R., C. A. Doswell III, M. P. Foster, and G. R. Woodall, 1994: The operational recognition of supercell thunderstorm environments and storm structures. *Wea. Forecasting*, **9**, 327–347, doi:10.1175/1520-0434(1994)009<0327:TOROST>2.0.CO;2.

Molthan, A. L., J. R. Bell, T. A. Cole, and J. E. Burks, 2014: Satellite-based identification of tornado damage tracks from the 27 April 2011 severe weather outbreak. *J. Oper. Meteor.*, **2**, 191–208, doi:10.15191/nwajom.2014.0216.

NCEI, 2016: Storm Events Database. NOAA/National Centers for Environmental Information. [Available online at https://www.ncdc.noaa.gov/stormevents/.]

NWS, 2011: Post-storm data acquisition. NWS Instruction 10-1604, 9 pp. [Available online at http://www.nws.noaa.gov/directives/sym/pd01016004curr.pdf.]

——, 2015: Impact Based Warnings national program. [Available online at http://www.weather.gov/impacts/.]

——, 2016: Storm Data preparation. NWS Instruction 10-1605, 110 pp. [Available online at http://www.nws.noaa.gov/directives/sym/pd01016005curr.pdf.]

Orlanski, I., 1975: A rational subdivision of scales for atmospheric processes. *Bull. Amer. Meteor. Soc.*, **56**, 527–530.

Przybylinski, R. W., 1995: The bow echo: Observations, numerical simulations, and severe weather detection methods. *Wea. Forecasting*, **10**, 203–218, doi:10.1175/1520-0434(1995)010<0203:TBEONS>2.0.CO;2.

ROC, 2012: Description document: Supplemental Adaptive Intra-Volume Low-Level Scan (SAILS). NWS/Radar Operations Center, 5 pp. [Available online at http://www.roc.noaa.gov/wsr88d/PublicDocs/NewTechnology/Supplemental_Adaptive_Intra_Volume_Low_Level_Scan_Description_Document_Final.pdf.]

——, 2014: Multiple Elevation Scan Option for SAILS (MESO-SAILS). NWS/Radar Operations Center, 27 pp. [Available online at https://www.roc.noaa.gov/WSR88D/PublicDocs/NewTechnology/MESO-SAILS_Description_Briefing_Jan_2014.pdf.]

Rotunno, R., J. B. Klemp, and M. L. Weisman, 1988: A theory for strong, long-lived squall lines. *J. Atmos. Sci.*, **45**, 463–485, doi:10.1175/1520-0469(1988)045<0463:ATFSLL>2.0.CO;2.

Ryzhkov, A. V., T. J. Schuur, D. W. Burgess, and D. S. Zrnić, 2005: Polarimetric tornado detection. *J. Appl. Meteor.*, **44**, 557–570, doi:10.1175/JAM2235.1.

Satellite Imaging Corporation, 2016: IKONOS satellite image of tornado damage in Oklahoma City. [Available online at http://www.satimagingcorp.com/gallery/ikonos/ikonos-tornadodamage-lg/.]

SBIR, 2015: NOAA FY 2016 SBIR solicitation. Small Business Innovation Research Program. [Available online at https://www.sbir.gov/node/831287.]

Schaumann, J. S., and R. W. Przybylinski, 2012: Operational application of 0-3 km bulk shear vectors in assessing quasi-linear convective system mesovortex and tornado potential. *26th Conf. on Severe Local Storms*, Nashville, TN, Amer. Meteor.

Soc., 142. [Available online at https://ams.confex.com/ams/26SLS/webprogram/Paper212008.html.]

Schenkman, A. D., and M. Xue, 2016: Bow-echo mesovortices: A review. *Atmos. Res.*, **170**, 1–13, doi:10.1016/j.atmosres.2015.11.003.

Schultz, C. J., and Coauthors, 2012: Dual-polarization tornadic debris signatures Part I: Examples and utility in an operational setting. *Electron. J. Oper. Meteor.*, **13** (9), 120–137. [Available online at http://nwafiles.nwas.org/ej/pdf/2012-EJ9.pdf.]

Schultz, L. A., K. Angle, T. Cole, K. Skow, J. Bell, A. L. Molthan, J. E. Burks, and K. M. McGrath, 2016: Applications of satellite imagery applications to assist in storm damage assessment. *Fourth Symp. on Building a Weather-Ready Nation: Enhancing Our Nation's Readiness, Responsiveness, and Resilience to High Impact Weather Events*, New Orleans, LA, Amer. Meteor. Soc., 10.2A. [Available online at https://ams.confex.com/ams/96Annual/webprogram/Paper286729.html.]

Skow, K., 2014: The art of storm surveying: Leveraging new datasets to document the 12 June 2013 tornadoes. *27th Conf. on Severe Local Storms*, Madison, WI, Amer. Meteor. Soc., JP12.170. [Available online at https://ams.confex.com/ams/27SLS/webprogram/Paper254329.html.]

——, 2015: An assessment of tornadic debris signatures observed in central Iowa. *19th Annual Severe Storms and Doppler Radar Conf.*, Ankeny, IA, Central Iowa NWA, 7. [Available online at http://www.iowa-nwa.com/conference/files/nwa_abs2015.pdf.]

——, 2016: Verification of tornadogenesis in high shear low CAPE environments using the correlation coefficient plume identification technique. *20th Annual Severe Storms and Doppler Radar Conf.*, Ankeny, IA, Central Iowa NWA, 6. [Available online at http://iowa-nwa.com/conference/files/2016_NWA_Agenda.pdf.]

Smull, B. F., and R. A. Houze Jr., 1987: Rear inflow in squall lines with trailing stratiform precipitation. *Mon. Wea. Rev.*, **115**, 2869–2889, doi:10.1175/1520-0493(1987)115<2869:RIISLW>2.0.CO;2.

Snow, J. T., C. R. Church, and B. J. Barnhart, 1980: An investigation of the surface pressure fields beneath simulated tornado cyclones. *J. Atmos. Sci.*, **37**, 1013–1026, doi:10.1175/1520-0469(1980)037<1013:AIOTSP>2.0.CO;2.

SPC, 2014: Storm reports from August 31, 2014. [Available online at http://www.spc.noaa.gov/climo/reports/140831_rpts.html.]

Spoden, P. J., R. A. Wolf, and L. R. Lemon, 2012: Operational uses of spectrum width. *Electron. J. Severe Storms Meteor.*, **7** (2). [Available online at http://www.ejssm.org/ojs/index.php/ejssm/article/view/86/70.]

Thompson, R. L., B. T. Smith, J. S. Grams, A. R. Dean, and C. Broyles, 2012: Convective modes for significant severe thunderstorms in the contiguous United States. Part II: Supercell and QLCS tornado environments. *Wea. Forecasting*, **27**, 1136–1154, doi:10.1175/WAF-D-11-00116.1.

Torres, S. M., and C. D. Curtis, 2007: Initial implementation of super-resolution data on the NEXRAD network. *23rd Int. Conf. on Interactive Information and Processing Systems (IIPS) for Meteorology, Oceanography, and Hydrology*, San Antonio, TX, Amer. Meteor. Soc., 5B.10. [Available online at http://ams.confex.com/ams/87ANNUAL/techprogram/paper_116240.htm.]

Trainor, J. E., D. Nagele, B. Philips, and B. Scott, 2015: Tornadoes, social science, and the false alarm effect. *Wea. Climate Soc.*, **7**, 333–352, doi:10.1175/WCAS-D-14-00052.1.

Trapp, R. J., and M. L. Weisman, 2003: Low-level mesovortices within squall lines and bow echoes. Part II: Their genesis and implications. *Mon. Wea. Rev.*, **131**, 2804–2823, doi:10.1175/1520-0493(2003)131<2804:LMWSLA>2.0.CO;2.

——, E. D. Mitchell, G. A. Tipton, D. W. Effertz, A. I. Watson, D. L. Andra Jr., and M. A. Magsig, 1999: Descending and nondescending tornadic vortex signatures detected by WSR-88Ds. *Wea. Forecasting*, **14**, 625–639, doi:10.1175/1520-0434(1999)014<0625:DANTVS>2.0.CO;2.

——, S. A. Tessendorf, E. S. Godfrey, and H. E. Brooks, 2005: Tornadoes from squall lines and bow echoes. Part I: Climatological distribution. *Wea. Forecasting*, **20**, 23–34, doi:10.1175/WAF-835.1.

USDA, 2015: National Agriculture Imagery Program (NAIP) information sheet. U.S. Dept. of Agriculture, 2 pp. [Available online at http://www.fsa.usda.gov/Internet/FSA_File/naip_info_sheet_2015.pdf.]

Van Den Broeke, M. S., 2015: Polarimetric tornadic debris signature variability and debris fallout signatures. *J. Appl. Meteor. Climatol.*, **54**, 2389–2405, doi:10.1175/JAMC-D-15-0077.1.

——, and S. T. Jauernic, 2014: Spatial and temporal characteristics of polarimetric tornadic debris signatures. *J. Appl. Meteor. Climatol.*, **53**, 2217–2231, doi:10.1175/JAMC-D-14-0094.1.

Van Tassel, E. L., 1955: The North Platte Valley tornado outbreak of June 27, 1955. *Mon. Wea. Rev.*, **83**, 255–264, doi:10.1175/1520-0493(1955)083<0255:TNPVTO>2.0.CO;2.

Wakimoto, R. M., 1983: The West Bend, Wisconsin storm of 4 April 1981: A problem in operational meteorology. *J. Appl. Meteor.*, **22**, 181–189, doi:10.1175/1520-0450(1983)022<0181:TWBWSO>2.0.CO;2.

——, and J. W. Wilson, 1989: Non-supercell tornadoes. *Mon. Wea. Rev.*, **117**, 1113–1140, doi:10.1175/1520-0493(1989)117<1113:NST>2.0.CO;2.

——, and Coauthors, 2016: Aerial damage survey of the 2013 El Reno tornado combined with mobile radar data. *Mon. Wea. Rev.*, **144**, 1749–1776, doi:10.1175/MWR-D-15-0367.1.

WDTD, 2016: Analyzing tornadic scale signatures. Warning Division Training Division. [Available online at http://www.wdtb.noaa.gov/courses/rac/severe/tornadic-signatures/presentation.html.]

Weisman, M. L., 1990: The numerical simulation of bow echoes. Preprints, *16th Conf. on Severe Local Storms*, Kananaskis Park, AB, Canada, Amer. Meteor. Soc., 428–433.

——, and R. J. Trapp, 2003: Low-level mesovortices within squall lines and bow echoes. Part I: Overview and sensitivity to environmental vertical wind shear. *Mon. Wea. Rev.*, **131**, 2779–2803, doi:10.1175/1520-0493(2003)131<2779:LMWSLA>2.0.CO;2.

Yuan, M., M. Dickens-Micozzi, and M. A. Magsig, 2002: Analysis of tornado damage tracks from the 3 May tornado outbreak using multispectral satellite imagery. *Wea. Forecasting*, **17**, 382–398, doi:10.1175/1520-0434(2002)017<0382:AOTDTF>2.0.CO;2.

Zrnić, D. S., and A. V. Ryzhkov, 1999: Polarimetry for weather surveillance radars. *Bull. Amer. Meteor. Soc.*, **80**, 389–406, doi:10.1175/1520-0477(1999)080<0389:PFWSR>2.0.CO;2.